

RESEARCH ARTICLE | DECEMBER 04 2023

Swirling instability of coaxial liquid jet in gas surroundings



Yiqian Xu (徐艺倩) ; Kai Mu (穆恺) ; Ran Qiao (乔然) ; Yanfeng Wu (吴燕峰) ; Ting Si (司廷)



Physics of Fluids 35, 122102 (2023)

<https://doi.org/10.1063/5.0178604>



View
Online



Export
Citation

CrossMark

Physics of Fluids

Special Topic: Overview of Fundamental
and Applied Research in Fluid Dynamics in UK

Submit Today

Swirling instability of coaxial liquid jet in gas surroundings

Cite as: Phys. Fluids **35**, 122102 (2023); doi: [10.1063/5.0178604](https://doi.org/10.1063/5.0178604)
 Submitted: 27 September 2023 · Accepted: 10 November 2023 ·
 Published Online: 4 December 2023



Yiqian Xu (徐艺倩), Kai Mu (穆恺), ^{a)} Ran Qiao (乔然), Yanfeng Wu (吴燕峰), and Ting Si (司廷)

AFFILIATIONS

Department of Modern Mechanics, University of Science and Technology of China, Hefei 230026, People's Republic of China

^{a)} Author to whom correspondence should be addressed: mukai@ustc.edu.cn

ABSTRACT

Linear instability analysis of an inviscid coaxial swirling jet is carried out by deriving an analytical dispersion relation of perturbation growth. The azimuthal Rankine vortex and the axial discontinuous velocity distribution are utilized as the jet basic flow. Due to the existence of double interfaces, the instability mechanisms of the coaxial swirling jet are much more complex than those of the single-layered swirling jet. The effects of control parameters (including the swirling ratio, the Weber number, the jet radius ratio, the velocity ratios between different fluids, and the azimuthal velocity jump at the inner interface) on the temporal instability of coaxial swirling jet with different azimuthal modes are studied. By comparing the growth rate of different azimuthal modes, the predominant mode that determines the jet breakup is identified. The results indicate that an increase in the swirling ratio, the Weber number, and the radius ratio can lead to predominant mode transition to larger azimuthal wavenumbers. The velocity ratio between the inner jet and the annular jet and that between the surrounding fluid and the annular jet mainly affect the axial Kelvin–Helmholtz (KH) instability. An enhancement of the KH instability leads to the jet breakup with smaller azimuthal wavenumbers. The azimuthal velocity jump affects the azimuthal KH instability, the centrifugal instability, and the Coriolis instability simultaneously, thus leading to a multiple influence on modes transition. The phase-diagram of the predominant modes is further given, showing that the relative importance between the centrifugal force and the interfacial tension plays a significant role on the transition of predominant modes.

Published under an exclusive license by AIP Publishing. <https://doi.org/10.1063/5.0178604>

I. INTRODUCTION

When one phase of the fluid is injected into another phase of the immiscible fluid through a capillary tube, a cylindrical jet can be formed due to the jet inertia force or other external forces. Applying circumferential rotation to the jet, a swirling jet can be further produced. The swirling jet is very common in nature such as tornadoes and cyclones. In these geophysical flows, vortex breakdown is a notable feature and has attracted much attention.^{1,2} The swirling jet is also widely utilized in engineering applications, such as the improvement of combustion efficiency^{3,4} and the noise reduction.^{5,6} The rotation of fluid can lead to abundant morphological structures and also affect the efficiency of jet atomization. Therefore, it is of great significance to investigate the evolution and instability characteristics of the swirling jet.

The instability of cylindrical jet without circumferential swirling has been studied for more than one hundred years. Rayleigh⁷ did the pioneering work to perform a temporal instability analysis on an inviscid liquid jet, showing that the hydrodynamic instability induced by surface tension is the main cause of jet breakup. Taking liquid viscosity

into account, he found that the disturbance wavelength on the jet surface can be infinite.⁸ Weber⁹ extended Rayleigh's theory by considering the effects of jet viscosity and surrounding environment, indicating that the most unstable wavelength increases with the jet viscosity. Taylor¹⁰ took the density of the surrounding gas into account. He found that the size of droplets generated by the jet breakup is much smaller than the diameter of the jet if the gas inertia force is large enough compared with the surface tension force. Reitz and Bracco¹¹ carried out a linear instability analysis on the liquid jet injecting into quiescent gas surroundings, in which the effects of liquid inertia, surface tension, viscous, and aerodynamic forces were considered. Through comparing the theoretical results with experimental measurements, they found that the theory can predict the breakup behaviors of liquid jet with low velocity very well. As the jet velocity increases to a large value, the theoretical results diverge from the experiments significantly. Apart from the temporal instability analysis, which does not consider the spatial propagation of perturbation waves, many studies also focus on the spatial and spatiotemporal instabilities of the liquid jet. Keller *et al.*¹² analyzed the spatial and spatiotemporal instabilities

of a semi-infinite jet and estimated the jet breakup length theoretically. Leib and Goldstein^{13,14} studied the transition between absolute instability and convective instability of the liquid jet, in which the liquid viscosity was taken into account. The influences of surface tension and velocity profiles were analyzed in detail. Up to now, there have been numerous books and review articles that focus on the instabilities of liquid jet, showing the jet breakup mechanisms systematically.^{15–18}

Comparing with the non-swirling cylindrical jet, the instability of the swirling liquid jet is much more complicated due to the addition of the azimuthal velocity component. The instability of the swirling jet has attracted considerable attention for decades. Some early studies considered the temporal and spatiotemporal instabilities of the well-known Batchelor vortex.^{19–21} Loiseleux *et al.*²² carried out a spatiotemporal instability analysis on the swirling jet based on azimuthal Rankine vortex (consisting of a core in solid body rotation surrounded by a potential flow with constant circulation) and axial discontinuous velocities. Neglecting the influence of surface tension and liquid viscosity, they derived an analytical dispersion relationship of perturbation growth. They also studied the transition between absolute and convective instabilities and the occurrence of vortex breakdown. Gallaire and Chomaz²³ considered a similar model but assumed a discontinuous azimuthal velocity on the jet interface. They indicated four different mechanisms on jet instability, which are the Coriolis effect brought by the rotation of vortex core, the centrifugal effect, and the axial and azimuthal Kelvin–Helmholtz (KH) instabilities caused by velocity difference. Parthasarathy and Subramaniam²⁴ considered the model in which an inviscid gas jet with constant angular velocity was injected into an irrotational co-flowing viscous liquid. They found that the swirling of gas jet would promote the instability, and the increase in angular velocity could lead to the occurrence of non-axisymmetric modes. Sun *et al.*²⁵ combined the normal mode method and the direct numerical simulation (DNS) to study the linear temporal instability of a swirling jet with centrifugally unstable Taylor vortex velocity profile. The results of DNS showed that the early evolution of the swirling jet is consistent with the prediction of linear instability analysis. Kubitschek and Weidman²⁶ brought in the Reynolds number and the Hocking number, which represents the ratio of the surface tension and the centrifugal force to describe the transition between the axisymmetric mode and non-axisymmetric modes with different azimuthal wavenumbers. The phase diagram of different instability modes was depicted in the Hocking number–Reynolds number space. Billant and Gallaire²⁷ derived a unified criterion for the centrifugal instability of the swirling jet and the pure vortex without axial flow, and the criterion was verified by numerical results. It was found that a vortex that is centrifugally unstable remains unstable in the presence of an axial flow. Jacques *et al.*²⁸ conducted linear and nonlinear stability analyses of rotating flows, considering the variation of axisymmetric liquid density. Apart from the theoretical analyses, experiments and numerical simulations were also widely utilized to investigate the instability of the swirling jet. Panda and McLaughlin²⁹ conducted experiments to study the jet instability with Reynolds number ranging from 20 000 to 60 000 and a certain swirling number of 0.5. Billant *et al.*¹ investigated the breakdown of the swirling water jet experimentally, considering the variation of swirling number and Reynolds number. Kubitschek and Weidman³⁰ performed experiments to observe the evolution and fragmentation process of a spatially non-uniform rotating liquid jet. The transition boundaries of different instability modes were found to

agree well with the theoretical prediction.²⁶ Recently, Sahu *et al.*³¹ carried out a numerical simulation to study the three-dimensional breakup morphology of the swirling jet, in which the liquid interface is captured by the volume of fluid (VOF) method. Schmidt and Oberleithner³² performed the linear and nonlinear simulations to study the dynamical behaviors of double liquid swirling jet. It is worth noting that the non-axisymmetric instability modes can also be induced by generating a liquid jet from noncircular orifice, and evolutions of the twisted jet with different azimuthal wavenumbers have been studied in recent years.^{33–35}

The swirling jet mentioned above only has a single-layered interface. If the liquid jet presents the core–shell double-layered structure (i.e., the coaxial swirling jet), the instability characteristics can be much more complicated due to the coupling effect of double interfaces. For the coaxial swirling jet, most of the existing studies focus on the gas–liquid–gas fluid system, in which an annular liquid sheet is surrounded by the inner and outer gas streams. Panchagnula *et al.*³⁶ established the model of an inviscid swirling liquid sheet. They ignored the azimuthal velocities of the inner and outer gas phases and analyzed the temporal instability of the liquid sheet through linear instability analysis. Liao *et al.*³⁷ considered the model where a non-swirling liquid sheet was subjected to the swirling inner and outer gas streams. The effects of flow parameters, fluid properties, and sheet geometries on the instability of the liquid sheet were investigated systematically. Yan *et al.*³⁸ carried out a three-dimensional linear instability analysis of a viscous annular swirling sheet with circumferential solid body rotation, and they ignored the viscosities and azimuthal velocities of both the inner and outer gas streams. They further considered the three-dimensional nonlinear spatial instability of the annular liquid sheet based on a similar model.³⁹ They found that the rotation could play a stabilizing effect if the rotational velocity of the liquid sheet is very small. In addition to the liquid sheet model mentioned above, Liu *et al.*⁴⁰ considered the situation in which the non-swirling liquid jet is surrounded by the swirling gas jet, which is injected into the outermost static air environment. They ignored the viscosities of liquid and gas phases and only considered a small velocity ratio between the liquid jet and the surrounding gas.

Despite the existing studies on the coaxial swirling jet, the instability mechanisms of the jet have not been revealed intensively. Previous research mainly focused on the instability characteristics of the annular liquid sheet, considering the swirling of either the liquid sheet or the gas phase. A systematical research concerning the effect of various control parameters on the instability of the coaxial swirling jet is still desired. Moreover, the transition mechanisms of the predominant azimuthal mode, which governs the breakup of the coaxial swirling jet, also need to be studied. All these limitations motivate the current study. In this work, we consider the instability of an inviscid coaxial liquid jet with circumferential swirling in gas surroundings. Our model considers the azimuthal Rankine vortex and the axial discontinuous velocity profile, which takes into account the swirling motion of all fluids. A linear temporal instability analysis is carried out to investigate the effects of various parameters on the jet instability systematically. This work is structured as follows. Section II gives the formulation of the problem, including the description of the physical model, the derivation, and the verification of the dispersion relation. Section III examines the effects of various parameters on the instability and mode transition of the coaxial swirling jet. Section IV provides the main conclusions of the study.

II. FORMULATION OF THE PROBLEM

A. Physical model and governing equations

An inviscid coaxial swirling jet is considered in the cylindrical coordinate (z, r, θ) , as sketched in Fig. 1. The inner jet with radius R_1 , density ρ_1 , and axial flow velocity $U_1(r)$ is surrounded by an annular jet with radius R_2 , density ρ_2 , and axial flow velocity $U_2(r)$. The surrounding fluid flows around the annular jet with density ρ_3 and axial flow velocity $U_3(r)$. The interfacial tensions of the inner jet and the annular jet are denoted by γ_1 and γ_2 , respectively. Circumferential swirling is added on the coaxial jet, and the azimuthal velocity components on the θ direction are denoted by $W_1(r)$, $W_2(r)$, and $W_3(r)$ for the inner jet, the annular jet, and the surrounding fluid, respectively. Several assumptions are made for our model: (i) all phases are incompressible Newtonian fluids, (ii) the effect of gravity and temperature is neglected, and (iii) there is no mass transfer across the interface.

The flow is governed by the Navier–Stokes equations, which contain the continuity equation and the momentum equation, i.e.,

$$\nabla \cdot \mathbf{u}_i = 0, \quad (1)$$

$$\frac{\partial \mathbf{u}_i}{\partial t} + \mathbf{u}_i \cdot \nabla \mathbf{u}_i = -\frac{1}{\rho_i} \nabla p_i, \quad (2)$$

where $i = 1, 2, 3$ represent the inner jet, the annular jet, and the driving fluid, $\mathbf{u}_i = [u_i, v_i, w_i]$ stands for the velocity components in the cylindrical coordinate (z, r, θ) , p_i denotes the pressure, and t denotes the time.

The corresponding boundary conditions are also given for the model. At the symmetric axis $r = 0$, the consistency conditions should be satisfied as follows:

$$u_i < \infty, \quad v_i < \infty, \quad w_i < \infty, \quad p_i < \infty, \quad (3)$$

$$\lim_{r \rightarrow 0} \frac{\partial u_i}{\partial r} = 0, \quad \lim_{r \rightarrow 0} \frac{\partial p_i}{\partial r} = 0. \quad (4)$$

At the inner and outer interfaces $r_j (=R_j + \eta_j, j = 1, 2)$, where η_j denotes the small perturbations of the interface position), the displacement continuity condition, the kinematic boundary condition, and the dynamic boundary condition should be satisfied as follows:

$$r_j(R_j^-) = r_j(R_j^+), \quad (5)$$

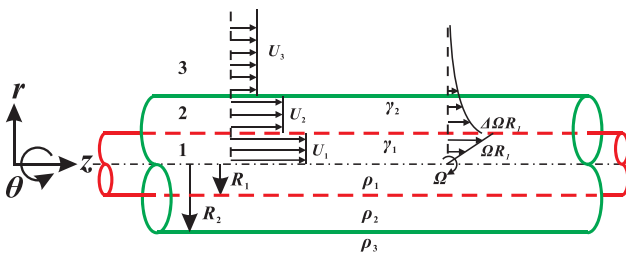


FIG. 1. Sketch of a coaxial swirling jet with axial discontinuous velocities and azimuthal Rankine vortex velocity profile in the cylindrical coordinate (z, r, θ) , where the inner jet with radius R_1 , density ρ_1 , axial velocity U_1 , and azimuthal velocity $W_1(r) (= \Omega r)$ is surrounded by the annular jet with radius R_2 , density ρ_2 , axial velocity U_2 , and azimuthal velocity $W_2(r) (= \Omega R_1^2 \Delta / r)$. The surrounding fluid flows with density ρ_3 , axial velocity U_3 , and azimuthal velocity $W_3(r) (= \Omega R_1^2 \Delta / r)$. The interfacial tensions of the inner jet and the annular jet are denoted by γ_1 and γ_2 , respectively.

$$v_j = \left(\frac{\partial}{\partial t} + \mathbf{u}_j \cdot \nabla \right) \eta_j, \quad (6)$$

$$p_j - p_{j+1} = \gamma_j \left(\frac{1}{r_j} - \frac{1}{r_j^2} \frac{\partial^2 \eta_j}{\partial \theta^2} - \frac{\partial^2 \eta_j}{\partial z^2} \right). \quad (7)$$

The infinity boundary condition at $r \rightarrow \infty$ is

$$u_3 < \infty, \quad v_3 < \infty, \quad w_3 < \infty, \quad p_3 < \infty. \quad (8)$$

B. Basic flow

In the linear instability analysis, the reasonable basic flow must be given first. For the theoretical model shown in Fig. 1, the basic velocity field is in the form of $\mathbf{U}_i = U_i \mathbf{e}_z + W_i \mathbf{e}_\theta$ ($i = 1, 2, 3$), where \mathbf{e}_z and \mathbf{e}_θ are the unit basic vectors in the z and θ directions, respectively. At the axial direction, we consider the plug flow with discontinuous velocity profiles. At the azimuthal direction, we consider the Rankine vortex flow with the vortex core inside the inner jet. The specific mathematical expressions of the basic velocity profiles are

$$U_1(r) = U_1, \quad W_1(r) = \Omega r \quad \text{at} \quad 0 \leq r \leq R_1, \quad (9)$$

$$U_2(r) = U_2, \quad W_2(r) = \frac{\Omega R_1^2 \Delta}{r} \quad \text{at} \quad R_1 < r \leq R_2, \quad (10)$$

$$U_3(r) = U_3, \quad W_3(r) = \frac{\Omega R_1^2 \Delta}{r} \quad \text{at} \quad r > R_2, \quad (11)$$

where U_1 , U_2 , and U_3 are the constant values representing the axial velocities, Ω is the angular velocity of the core rotation, and Δ is the parameter that reflects the azimuthal velocity jump at the inner jet interface. When $\Delta = 1$, the azimuthal velocity is continuous at the interface. The azimuthal velocity decreases abruptly at the interface when $0 \leq \Delta < 1$, while it increases at the interface when $\Delta > 1$. Under the Rankine vortex flow, the vorticity can be estimated by $\omega_i = \nabla \times \mathbf{U}_i$, i.e.,

$$\omega_1 = 2\Omega \mathbf{e}_z \quad \text{at} \quad 0 < r \leq R_1, \quad (12)$$

$$\omega_i = 0, \quad i = 2, 3 \quad \text{at} \quad r > R_1. \quad (13)$$

Therefore, the flow is rotational in the inner jet and irrotational in the annular jet and the surrounding flow. Similar to the previous study, which considers the instability of a single-layered swirling jet,²³ our model contains different instability mechanisms for the coaxial swirling jet, including the axial and azimuthal KH instabilities, the centrifugal instability, and the instability caused by the Coriolis force. The KH instabilities are caused by the discontinuity of the axial and azimuthal velocities at the interface, respectively. The centrifugal instability is active as $\Delta < 1$. In this situation, the circulation decreases suddenly between the inner jet and the annular jet. The instability generated by the Coriolis force is caused by the solid rotation of the vortex core.

C. Derivation of the dispersion relation

The flow variables and the interface positions are all divided into basic quantities and infinitesimal disturbances in the linear instability analysis. Consequently, the interface positions, the velocity components at the axial, radial, and azimuthal directions, and the pressure can be represented as

$$\begin{aligned} r_j &= R_j + \eta_j, \quad j = 1, 2, \\ \mathbf{u}_i &= \mathbf{U}_i + \tilde{\mathbf{u}}_i, \quad p_i = P_i + \tilde{p}_i, \quad i = 1, 2, 3, \end{aligned} \quad (14)$$

where U_i , P_i , and R_j are the basic flow states and $\tilde{\mathbf{u}}_i$, \tilde{p}_i , and η_j are the disturbances.

Substituting Eq. (14) into Eqs. (1)–(10) and neglecting the high-order terms, the linearized disturbance equations and boundary conditions can be derived as

$$\nabla \cdot \tilde{\mathbf{u}}_i = 0, \quad i = 1, 2, 3, \quad (15)$$

$$\frac{\partial \tilde{\mathbf{u}}_i}{\partial t} + \tilde{\mathbf{u}}_i \cdot \nabla \mathbf{U}_i + \mathbf{U}_i \cdot \nabla \tilde{\mathbf{u}}_i = -\frac{1}{\rho_i} \tilde{p}_i, \quad i = 1, 2, 3. \quad (16)$$

At the axis of symmetry $r = 0$:

$$\tilde{u}_1 < \infty, \quad \tilde{v}_1 < \infty, \quad \tilde{w}_1 < \infty, \quad \tilde{p}_1 < \infty, \quad (17)$$

$$\lim_{r \rightarrow 0} \frac{\partial \tilde{\mathbf{u}}_1}{\partial \theta} = 0, \quad \lim_{r \rightarrow 0} \frac{\partial \tilde{p}_1}{\partial \theta} = 0. \quad (18)$$

At the inner and the outer interfaces ($r_j = R_j + \eta_j$, $j = 1, 2$):

$$\eta_j(R_j^-) = \eta_j(R_j^+), \quad (19)$$

$$\tilde{\mathbf{v}}_j = \left(\frac{\partial}{\partial t} + \mathbf{U}_j \cdot \nabla \right) \eta_j, \quad (20)$$

$$\left(-\frac{dP_{j+1}}{dr} + \frac{dP_j}{dr} \right) \eta_j + \tilde{p}_j - \tilde{p}_{j+1} = -\gamma_j \left(\frac{1}{R_j^2} + \frac{\partial^2}{R_j^2 \partial \theta^2} + \frac{\partial^2}{\partial z^2} \right) \eta_j. \quad (21)$$

At the infinity position ($r \rightarrow \infty$):

$$\tilde{u}_3 \rightarrow 0, \quad \tilde{v}_3 \rightarrow 0, \quad \tilde{w}_3 \rightarrow 0, \quad \tilde{p}_3 \rightarrow 0. \quad (22)$$

The normal mode method is utilized to analyze the growth of disturbances. In this method, the disturbances $\tilde{\mathbf{u}}_i = (\tilde{u}_i, \tilde{v}_i, \tilde{w}_i)$, \tilde{p}_i , and η_j are all expressed in the Fourier form

$$\begin{aligned} \{\tilde{u}_i, \tilde{v}_i, \tilde{w}_i, \tilde{p}_i\} &= \{\hat{u}_i(r), \hat{v}_i(r), \hat{w}_i(r), \hat{p}_i(r)\} e^{i(kz + m\theta - \omega t)}, \\ \tilde{\eta}_j &= \hat{\eta}_j e^{i(kz + m\theta - \omega t)}, \end{aligned} \quad (23)$$

where k is the axial wavenumber, m is the azimuthal wavenumber, and $\omega (= \omega_r + i\omega_i)$, where i represents the imaginary unit, is the complex frequency. In the temporal instability analysis, m is an integer and k is a real number. The real and imaginary parts of ω (i.e., ω_r and ω_i) stand for the frequency and the growth rate of disturbance, respectively. If $\omega_i < 0$ for all values of k , the jet is stable invariably; if $\omega_i > 0$ for some values of k , the jet is unstable. The jet is neutral stable at $\omega_i = 0$ as the disturbances neither grow nor decay with time. The variation of m stands for different azimuthal modes. $m = 0$ represents the axisymmetric mode in which the jet evolves with axisymmetric perturbation, and $m \geq 1$ stands for the helical modes in which the jet develops under non-axisymmetric disturbances. Without the loss of generality, the present work mainly focuses on the instability characteristics for modes $m = 0-5$.

Substituting Eq. (23) into Eqs. (15)–(22), the dispersion relation between ω and k can be obtained. Choosing the annular jet as the characteristic phase and R_2 , U_2 , R_2/U_2 , $R_2 U_2^2$, ρ_2 , γ_2 as the characteristic length, velocity, time, pressure, density, and surface tension, respectively, the dimensionless parameters involved in the theoretical model can be defined, including the swirling ratio $S = \Omega R_2/U_2$, the Weber number $We = \rho_2 U_2^2 R_2/\gamma_2$, the jet radius ratio $\kappa = R_1/R_2$, the velocity

ratios $V = U_1/U_2$ and $W = U_3/U_2$, the density ratios $J = \rho_1/\rho_2$ and $Q = \rho_3/\rho_2$, the surface tension ratio $\tau = \gamma_1/\gamma_2$, the complex frequency $\beta = \omega R_2/U_2$, and the axial wavenumber $\alpha = kR_2$. Therefore, the dimensionless dispersion relation can be derived as

$$\begin{aligned} &[T_1 + (\beta - \alpha - m\Delta S)^2 H_2] \cdot [T_2 + (\beta - \alpha - m\Delta S \kappa^2)^2 H_4] \\ &= (\beta - \alpha - m\Delta S \kappa^2)^2 (\beta - \alpha - m\Delta S)^2 H_3 H_5, \end{aligned} \quad (24)$$

where

$$\begin{aligned} T_1 &= \frac{J t_1 (\beta - \alpha V - mS)^2 J_m(\beta_1 R_1)}{\sqrt{t_1} J'_m(\beta_1 R_1) - \frac{2mS J_m(\beta_1 R_1)}{\kappa \alpha (\beta - \alpha V - mS)}} \\ &+ \frac{\alpha \tau (m^2 - 1 + \kappa^2 \alpha^2)}{We \kappa^2} + \kappa \alpha S^2 (\Delta^2 - J), \end{aligned}$$

$$\begin{aligned} T_2 &= Q(\beta - \alpha W - m\Delta S \kappa^2)^2 \frac{K_m(\alpha)}{K'_m(\alpha)} \\ &+ \frac{\alpha (m^2 - 1 + \alpha^2)}{We} + \alpha \Delta^2 \kappa^2 S^2 (Q - 1), \end{aligned}$$

$$t_1 = \frac{4S^2}{(\beta - \alpha V - mS)^2} - 1, \quad \beta_1 R_1 = \kappa \alpha \sqrt{\frac{4S^2}{(\beta - \alpha V - mS)^2} - 1},$$

$$\begin{aligned} H_1 &= I'_m(\alpha) K'_m(\kappa \alpha) - I'_m(\kappa \alpha) K'_m(\alpha), \\ H_2 &= K_m(\kappa \alpha) I'_m(\alpha) - K'_m(\alpha) I_m(\kappa \alpha), \\ H_3 &= K_m(\kappa \alpha) I'_m(\kappa \alpha) - K'_m(\kappa \alpha) I_m(\alpha), \\ H_4 &= K_m(\alpha) I'_m(\kappa \alpha) - K'_m(\kappa \alpha) I_m(\alpha), \\ H_5 &= K_m(\alpha) I'_m(\alpha) - K'_m(\alpha) I_m(\alpha). \end{aligned}$$

The derivation details are given in the Appendix. In the dispersion relation, the imaginary part of β (denoted by β_i) demonstrates the nondimensional disturbance growth rate, which will be analyzed in detail in Sec. III.

D. Validation of the dispersion relation

To verify the correctness of the dispersion relation, the physical model can be simplified to compare with the previous studies. Specifically, the coaxial swirling jet degenerates to single-layered swirling jet with only one interface. In this situation, the annular jet is ignored and the region of the driving fluid is $r > R_1$. The dynamic boundary condition on the interface can be described as

$$\frac{dP_1(R_1)}{dr} - \frac{dP_3(R_1)}{dr} + \hat{p}_1(R_1) - \hat{p}_3(R_1) = \gamma_1 \left(\frac{m^2 - 1}{R_1^2} + k^2 \right) \hat{\eta}_1. \quad (25)$$

For the simplified single-layered swirling jet, we choose the radius and velocity of the jet (i.e., R_1 and U_1) as the characteristic scales; thus, the nondimensionalized dispersion relation can be obtained with the form

$$\begin{aligned} &\frac{(\beta - \alpha - mS)^2 \sqrt{t_1} J_m(\beta_1 R_1)}{J'_m(\beta_1 R_1) - \frac{2mS J_m(\beta_1 R_1)}{\alpha (\beta - \alpha - mS) \sqrt{t_1}}} + \frac{\alpha (m^2 - 1 + \alpha^2)}{We} \\ &+ \alpha S^2 (J \Delta^2 - 1) + \frac{J K_m(\alpha)}{K'_m(\alpha)} (\beta - \alpha W - m\Delta S)^2 = 0, \end{aligned} \quad (26)$$

where

$$J = \frac{\rho_3}{\rho_1}, \quad W = \frac{U_3}{U_1}, \quad We = \frac{\rho_1 U_1^2 R_1}{\gamma_1}, \quad t_1 = \frac{4a^2}{(\beta - \alpha - mS)^2} - 1, \\ S = \frac{\Omega R_1}{U_1}, \quad \beta_1 R_1 = \alpha \sqrt{\frac{4S^2}{(\beta - \alpha - mS)^2} - 1}, \quad \alpha = kR_1, \quad \beta = \frac{\omega R_1}{U_1}.$$

Setting $\Delta = 1$ and ignoring the interfacial tension ($We \rightarrow \infty$), Eq. (26) is exactly the same as that obtained by Loiseleux *et al.*²²

The current model can also be reduced to the coaxial jet without circumferential swirling by setting $S = 0$. In this way, the dispersion relation of Eq. (24) can be simplified as

$$[T_1 + (\beta - \alpha)^2 H_2] \cdot [T_2 + (\beta - \alpha)^2 H_4] = (\beta - \alpha)^4 H_3 H_5, \quad (27)$$

where

$$T_1 = iJ(\beta - \alpha V)^2 \frac{J_m(\beta_1 R_1)}{J'_m(\beta_1 R_1)} + \frac{\alpha \tau (m^2 - 1 + \kappa^2 \alpha^2)}{We \kappa^2}, \\ T_2 = Q(\beta - \alpha W)^2 \frac{K_m(\alpha)}{K'_m(\alpha)} + \frac{\alpha (m^2 - 1 + \alpha^2)}{We}.$$

It is worth noting that the previous work carried out by Li *et al.*⁴¹ has considered the inviscid coaxial jet instability under an external electric field. By setting the parameters related to the electric field to zero, a same dispersion relation with Eq. (27) can be obtained.

III. TEMPORAL INSTABILITY ANALYSIS

To investigate the influence of control parameters on the instability of the coaxial swirling jet, a reference state must be given first. The reference state should correspond to the real flow conditions to ensure the rationality of the theoretical results. For the materials of the coaxial jet, the silicone oil, distilled water, and air are chosen as the inner jet, the annular jet, and the surrounding fluid, respectively. This combination of fluids has been widely used in previous experimental^{42,43} and theoretical⁴⁴ studies on the instability of non-swirling coaxial jet. The densities and dynamic viscosities of fluids correspond to $\rho_1 = 0.84 \times 10^3$, $\rho_2 = 10^3$, $\rho_3 = 1.29 \text{ kg/m}^3$, and $\mu_1 = 10^{-3}$, $\mu_2 = 10^{-3}$, $\mu_3 = 2 \times 10^{-5} \text{ Pas}$, respectively. The interfacial tensions of the inner and outer interfaces are $\gamma_1 = 30$ and $\gamma_2 = 72 \text{ mN/m}$, respectively. Similar to the experimental study that considers the single-layered swirling jet,³⁰ we choose the characteristic length as $R_2 = 5 \text{ mm}$ and the characteristic velocity as $U_2 = 2 \text{ m/s}$. For the reference state, we consider the annular velocity as $\Omega = 200 \text{ rad/s}$ and the inner jet radius as $R_1 = 3 \text{ mm}$. We also consider that the axial velocity of the inner jet is slightly faster than that of the annular jet ($U_1 = 1.1 \times U_2$), and the coaxial liquid jet moves in static gas surroundings ($U_3 = 0$). Moreover, the azimuthal velocity is assumed to be continuous at the inner interface. Therefore, the values of the typical dimensionless parameters are calculated as the reference state in the following:

$$S = 0.5, \quad We = 278, \quad \kappa = 0.6, \quad V = 1.1, \quad W = 0, \quad J = 0.84, \\ Q = 0.0013, \quad \tau = 0.42, \quad \text{and} \quad \Delta = 1.$$

To illustrate the rationality of the inviscid assumption, the Reynolds numbers of the coaxial swirling jet are also calculated. Choosing the axial velocities as the characteristic scales, the Reynolds number of the inner jet is $Re_{i1} = \rho_1 U_1 R_1 / \mu_1 = 5544$ and that of the

annular jet is $Re_{a1} = \rho_2 U_2 R_2 / \mu_2 = 10\,000$. Choosing the azimuthal velocities as the characteristic scales, the Reynolds number of the inner jet is $Re_{i2} = \rho_1 \Omega R_1^2 / \mu_1 = 1512$ and that of the annular jet is $Re_{a2} = \rho_2 (\Omega R_1) R_2 / \mu_2 = 3000$. As the Reynolds numbers representing the axial and circumferential flows are at the order of $\sim 10^3$, the inviscid model as well as the discontinuous velocity profiles [see Eqs. (9)–(11)] can give a similar prediction of perturbation growth comparing with the full viscous model.^{45–47}

In this section, we analyze the effects of dimensionless control parameters S , We , κ , V , W , and Δ on the temporal instability of the coaxial swirling jet, considering both the axisymmetric mode ($m = 0$) and the helical modes with different azimuthal wavenumbers ($m = 1-5$). We also study the mode competition by comparing the maximum growth rates of different azimuthal modes and determine the predominant instability mode.

A. Effect of the swirling ratio S

The swirling ratio S reflects the degree of the inner jet rotation, which is one of the most prominent parameters for the coaxial swirling jet. Figures 2(a)–2(f) show the perturbation growth rates β_i for azimuthal mode from $m = 0$ to 5 as S varies. For a certain growth rate curve, as sketched in Fig. 2(a), the cutoff wavenumber $\alpha_{\text{cut-off}}$ indicates the unstable region of perturbation. Since the perturbation grows exponentially in the form of $\sim e^{\beta_i t}$, the maximum growth rate $\beta_{i\text{max}}$ dominates the jet instability among all perturbations in the unstable region, and the corresponding wavenumber α_{max} (referred to as the most unstable wavenumber hereafter) determines the size of the resulting droplets. It is clear that the helical modes with $m \geq 2$ only become unstable as S reaches some critical values. For example, the unstable growth rate curves only occur as $S \geq 0.2$ for mode $m = 2$ [see Fig. 2(c)], and the unstable growth rate curves occur as $S \geq 0.4$ for modes $m = 3 \sim 5$, as shown in Figs. 2(d)–2(f), respectively. Moreover, for the axisymmetric mode with $m = 0$ [see Fig. 2(a)], the perturbation growth rate corresponds to zero invariably when $\alpha = 0$. However, the coaxial swirling jet with $S > 0$ is unstable with $\beta_i > 0$ at $\alpha = 0$ under helical modes $m = 1-5$ [see Figs. 2(b)–2(f)]. This observation indicates that the coaxial swirling jet is unstable at infinite perturbation wavelength as the dimensionless wavelength λ is inversely proportional to the wavenumber ($\lambda = 2\pi/\alpha$).

Figure 2(a) shows that the cutoff wavenumber of the axisymmetric mode decreases slightly when S increases from 0 to 0.2 and increases significantly when S further increases from 0.2 to 1. This indicates that the unstable wavenumber region narrows first and then extends to the larger wavenumber as S gradually increases. A larger cutoff wavenumber brings in more perturbation wave with shorter wavelength into instability. The maximum growth rate of axisymmetric mode changes slightly between $S = 0$ and 0.2 but increases rapidly as S increases from 0.2 to 1, indicating that the swirling can promote the jet instability of axisymmetric mode significantly. With the increase in S , the most unstable wavenumber first decreases and then increases observably. A larger value of α_{max} results in a smaller wavelength of the interface perturbation on the jet breakup. Overall, an enhancement of circumferential swirling can lead to the formation of smaller droplets under the axisymmetric mode. For the helical mode $m = 1$ shown in Fig. 2(b), the cutoff wavenumber increases as S increases, suggesting a widened instability region of wavelength. The maximum growth rate also increases with the increase in S , while the most unstable

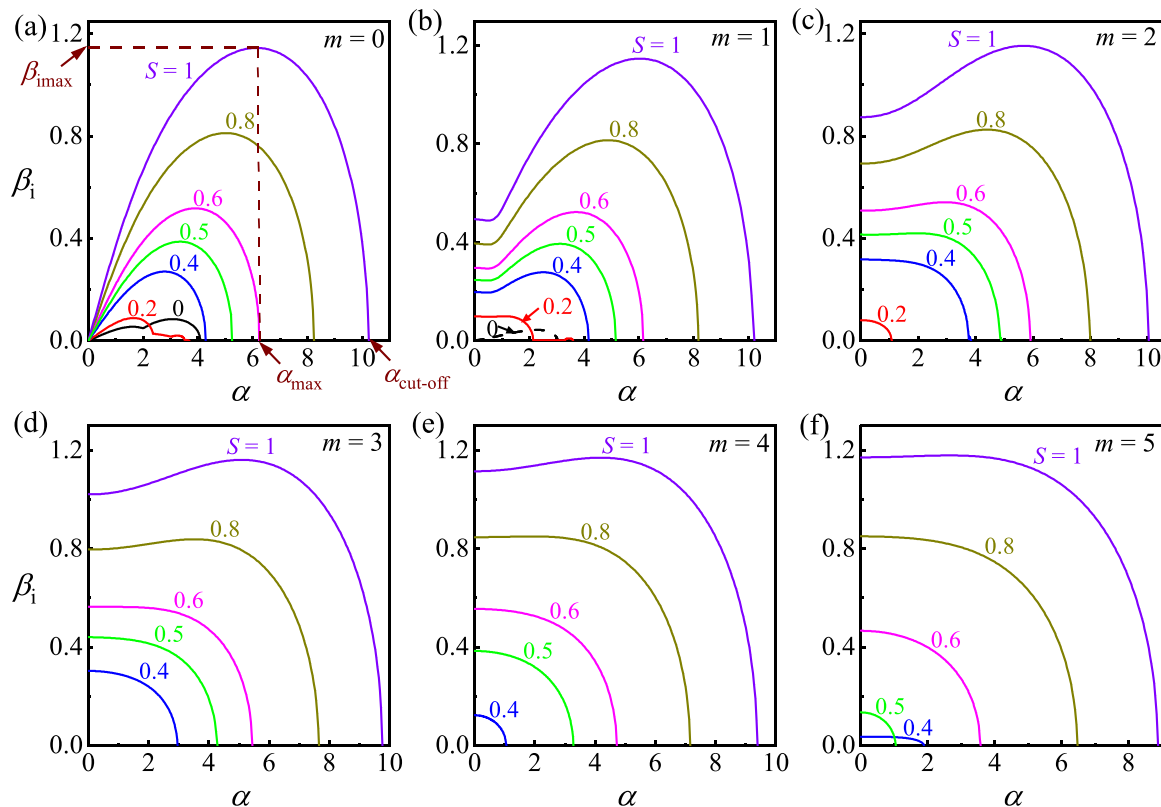


FIG. 2. Perturbation growth rate β_i vs wavenumber α for different azimuthal modes as S gradually changes ($S = 0, 0.2, 0.4, 0.5, 0.6, 0.8$, and 1 , respectively): (a) $m = 0$, (b) $m = 1$, (c) $m = 2$, (d) $m = 3$, (e) $m = 4$, and (f) $m = 5$.

wavenumber first decreases as S increases from 0 to 0.2 and then increases as S keeps increasing from 0.2 to 1 . For the helical mode $m = 2-4$ shown in Figs. 2(c)–2(e), it is observed that the increase in S will increase the cutoff wavenumber and the maximum growth rate simultaneously, indicating that a widened unstable perturbation wave range and a more unstable jet can be obtained. The most unstable wavenumbers for the modes $m = 2-4$ first keep constant at zero and then increase with the increase in S . For the helical mode $m = 5$ shown in Fig. 2(f), the cutoff wavenumber first decreases as S increases from 0.4 to 0.5 and then increases as S keeps increasing. Similar to the situations of modes $m = 2-4$, the maximum growth rate of $m = 5$ increases with the increase in S , while the most unstable wavenumber first keeps constant at zero and then increases as S increases.

To gain more details about the effect of S on the jet instability, the maximum perturbation growth rates $\beta_{i\max}$ and the most unstable wavenumbers α_{\max} for different azimuthal modes ($m = 0-5$) as S increases from 0 to 1 are given in Figs. 3(a) and 3(b), respectively. Figure 3(a) shows that both the axisymmetric mode $m = 0$ and the helical modes $m = 1-5$ present an overall increasing tendency of $\beta_{i\max}$ as S gradually increases, suggesting that the enhancement of swirl can promote the jet instability. Generally, the azimuthal mode corresponding to the maximum value of $\beta_{i\max}$ can dominate the jet breakup, which is considered as the predominant mode. Therefore, the predominant mode under certain S can be identified by comparing the values of $\beta_{i\max}$ between different azimuthal modes. In this way, the

predominate mode as S gradually varies can be obtained, and the results are displayed in Fig. 3(a) by the red numbers. It can be seen clearly that there is a step-by-step transition of the predominant mode from $m = 0$ to $m = 5$ as S gradually increases, indicating that the enhancement of swirling can lead to the jet breakup with larger azimuthal wavenumber. It should be noted that in previous experimental and theoretical studies of single-layered swirling jet, a similar tendency of the predominant mode transition has also been observed.^{26,30} As $\Delta = 1$ for the cases considered here, the coaxial jet is centrifugal stable.²³ The increase in S mainly enhances the instability caused by the Coriolis force, which contributes to the azimuthal mode transition. Figure 3(b) displays the effect of S on the most unstable wavenumbers α_{\max} for different modes ($m = 0-5$). The most unstable wavenumbers of the axisymmetric mode with $m = 0$ and the helical mode with $m = 1$ decrease first and then increase rapidly with the increase in S , whereas the most unstable wavenumbers of $m = 2-5$ almost maintain at zero first and then increase quickly as S becomes larger than some critical values. As the increase in S leads to the transition between different modes, we also highlight the α_{\max} , which corresponds to the predominate mode as solid symbols in Fig. 3(b), and the solid symbols are connected with a black thick dashed line. It is observed that the variation tendency of α_{\max} of the predominate mode shows a non-monotonic manner. Overall, with the increase in S , α_{\max} decreases at first and maintains relatively low values and then it increases as S keeps increasing to large values.

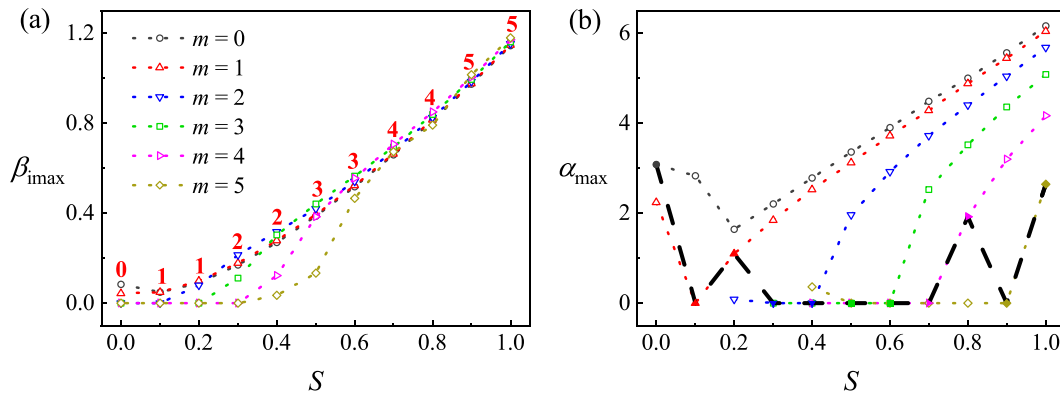


FIG. 3. (a) Maximum perturbation growth rate β_{\max} for different azimuthal modes as S varies. The predominant mode is indicated by the red numbers. (b) Most unstable wavenumber α_{\max} for different azimuthal modes as S varies. The most unstable wavenumbers corresponding to the predominant mode at different S are depicted by the solid symbols and connected by the black thick dashed line.

B. Effect of the Weber number We

The Weber number reflects the relative importance between the inertia force and the interfacial tension. Figures 4(a)–4(f) show the perturbation growth rates β_i for azimuthal modes $m = 0$ –5 as We varies. Similar to the situation of S varying, the helical modes with $m \geq 2$ only become unstable as We increases beyond the critical values.

Specifically, the modes $m = 2$ and 3 remain stable when $We = 1$ and 10, and the modes $m = 4$ and 5 remain stable when $We = 1, 10$, and 100. It can be seen from Fig. 4(a) that the cutoff wavenumber of the axisymmetric mode ($m = 0$) keeps almost constant close to 1 at a relatively small We (e.g., $We = 1, 10$), indicating that the jet breakup presents the Rayleigh mode (with the resulting drop size at the order

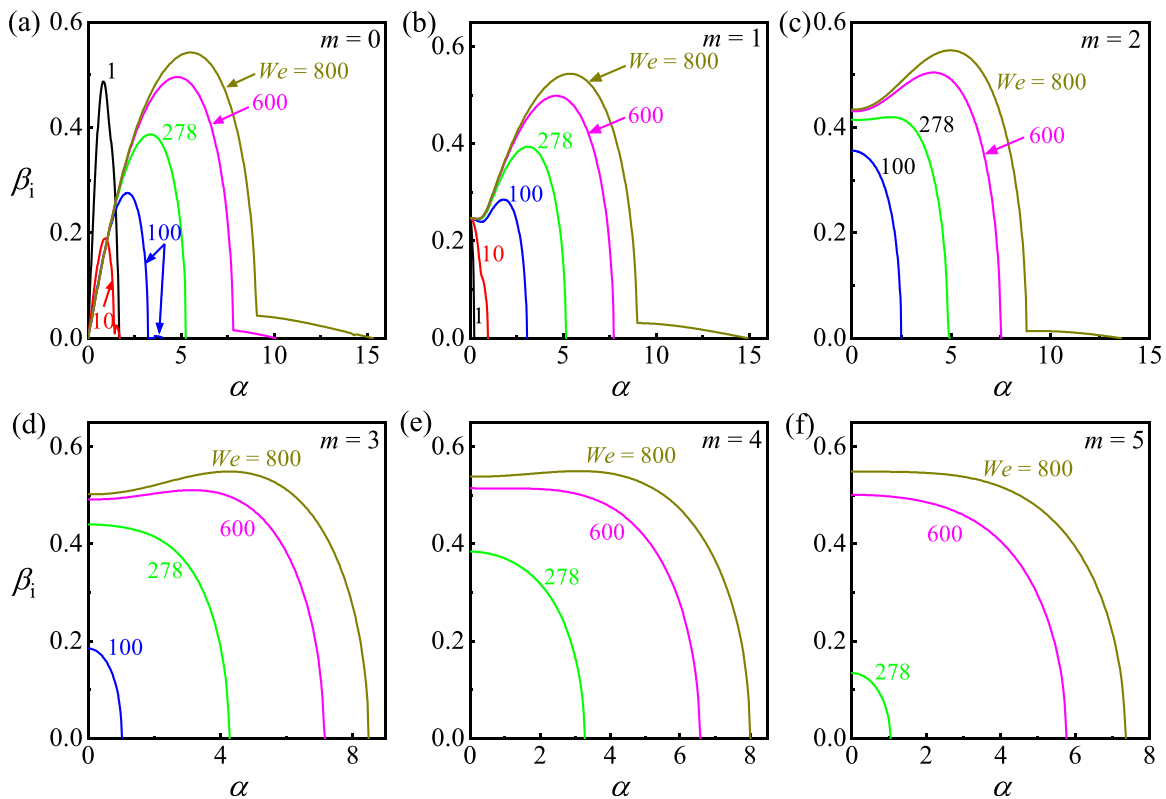


FIG. 4. Perturbation growth rate β_i vs wavenumber α for different azimuthal modes as We gradually changes ($We = 1, 10, 100, 278, 600$, and 800 , respectively): (a) $m = 0$, (b) $m = 1$, (c) $m = 2$, (d) $m = 3$, (e) $m = 4$, and (f) $m = 5$.

of the jet diameter). As We increases from 10 to 800, the cutoff wavenumber gradually gets larger, indicating that the unstable region is extended to perturbations with much shorter wavelength. The maximum growth rate β_{imax} of $m=0$ decreases first and then increases with the increase in We , suggesting that We has a dual effect on the axisymmetric mode. The effect of We on the most unstable wavenumber is similar to that of the cutoff wavenumber under the axisymmetric perturbation. When We increases from 1, α_{max} keeps almost constant first and then increases observably. It can be seen from Fig. 4(a) that as We increases to large values [e.g., $We \sim O(10^2)$], the cutoff wavenumber and the most unstable wavenumber can be relatively large, which indicates that the jet breakup presents the Taylor mode (with the drop size much smaller than the jet diameter). Compared with the Rayleigh mode where the interfacial tension dominates the jet instability, the KH instability plays a more significant role in the Taylor mode.^{15,17} As for the helical mode $m=1$ shown in Fig. 4(b), it is clear that $\alpha_{\text{cut-off}}$ increases with the increase in We , which leads to a wider unstable perturbation region. The maximum growth rate β_{imax} and the most unstable wavenumber α_{max} keep constant as $We \leq 10$ and then increase with the increase in We . For helical modes $m=2-5$ shown in Figs. 4(c)–4(f), the increase in We can lead to larger values of $\alpha_{\text{cut-off}}$ and β_{imax} . Therefore, the unstable perturbation region can extend to larger wavenumbers and the jet instability will be enhanced as We increases. The overall variation tendencies of the most unstable wavenumbers between modes $m=2-5$ are rather similar, where α_{max} keeps almost constant at zero first and then increases with We as the value of We exceeds the critical values.

The maximum perturbation growth rates β_{imax} and the most unstable wavenumbers α_{max} for azimuthal modes $m=0$ to 5 as We increases from 1 to 800 are presented in Figs. 5(a) and 5(b), respectively. As we have pointed out before, the effect of We on the axisymmetric mode $m=0$ is dualistic, where the values of β_{imax} first decrease and then increase with the increase in We , as shown in Fig. 5(a). For the helical modes $m=1-5$, β_{imax} maintains constant as low values of We but increases with We significantly as We exceeds the critical values. The red numbers in Fig. 5(a) denote the predominant modes, which determine the jet breakup at different Weber numbers. Overall, the predominant mode gradually trans from $m=0$ to 4 with the continuous increase in We , indicating that the weakening of the interfacial

tension can promote the occurrence of helical modes with larger azimuthal wavenumber. The variation of the most unstable wavenumbers is shown in Fig. 5(b). For modes $m=0-4$, it is observed that the value of α_{max} first maintains constant and then increases quickly as We increases. However, α_{max} keeps constant at zero within the range $1 \leq We \leq 800$ for mode $m=5$. The most unstable wavenumbers of the predominant mode at different We are highlighted with solid symbols and connected with the black thick dashed line. As We gradually increases, α_{max} first decreases from a small value to zero and then increases significantly at large We , implying a decrease in the droplet size as the jet inertia is sufficiently strong compared with the interfacial tension.

C. Effect of the jet radius ratio κ

The radius ratio of the inner and the annular jet κ reflects the size of the vortex core, which also affects the swirling characteristics of the jet significantly. Figures 6(a)–6(f) show the perturbation growth rates β_i for different azimuthal modes ($m=0-5$) as κ gradually increases. It is observed that the helical modes with $m \geq 2$ can only become unstable as κ reaches the critical values. For example, modes $m=2$ and 3 maintain stable when $\kappa=0.1$ and 0.2, and modes $m=4$ and 5 maintain stable as $\kappa=0.1, 0.2$, and 0.4, respectively. For the axisymmetric mode $m=0$ shown in Fig. 6(a), it is found that the cutoff wavenumber $\alpha_{\text{cut-off}}$, the maximum growth rate β_{imax} , and the most unstable wavenumber α_{max} all decrease first and then gradually increase with the increase in κ , indicating a dual effect of κ on the jet instability. For the helical modes $m=1-5$ shown in Figs. 6(b)–6(f), it is observed that $\alpha_{\text{cut-off}}$ and β_{imax} both increase with the increase in κ , suggesting that an increase in the vortex core radius can extend the unstable wavenumber region and also promote the jet instability. The corresponding most unstable wavenumbers of $m=1$ and 2 maintain at zero first and then increase with the increase in κ , while the most unstable wavenumbers of $m=3, 4$, and 5 are equal to zero invariably.

The maximum perturbation growth rates β_{imax} and the most unstable wavenumbers α_{max} for different azimuthal modes ($m=0-5$) as κ changes from 0.1 to 0.9 are displayed in Figs. 7(a) and 7(b), respectively. Figure 7(a) shows that κ has a dual effect on jet instability for mode $m=0$, where β_{imax} reaches its minimum at $\kappa=0.2$.

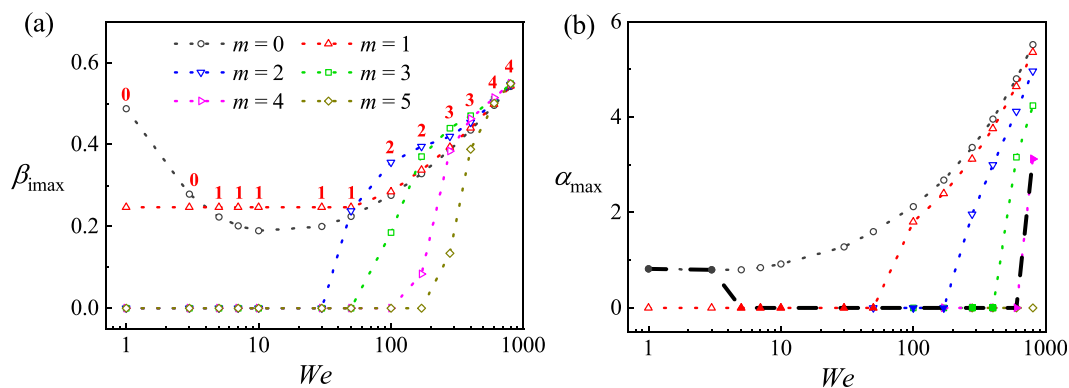


FIG. 5. (a) Maximum perturbation growth rate β_{imax} for different azimuthal modes as We varies. The predominant mode is indicated by the red numbers. (b) Most unstable wavenumber α_{max} for different azimuthal modes as We changes. The most unstable wavenumbers corresponding to the predominant mode at different We are depicted by the solid symbols and connected by the black thick dashed line.

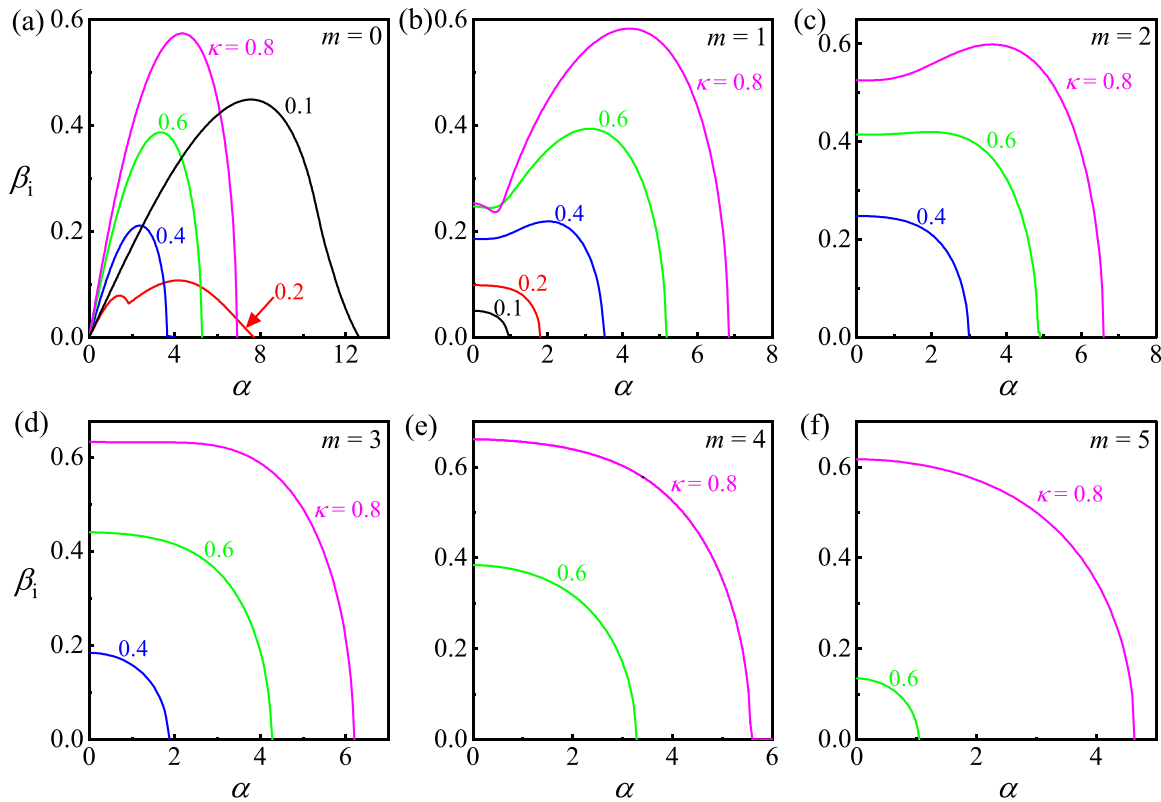


FIG. 6. Perturbation growth rate β_i vs wavenumber α for different azimuthal modes as κ gradually changes ($\kappa = 0.1, 0.2, 0.4, 0.6$, and 0.8 , respectively): (a) $m = 0$, (b) $m = 1$, (c) $m = 2$, (d) $m = 3$, (e) $m = 4$, and (f) $m = 5$.

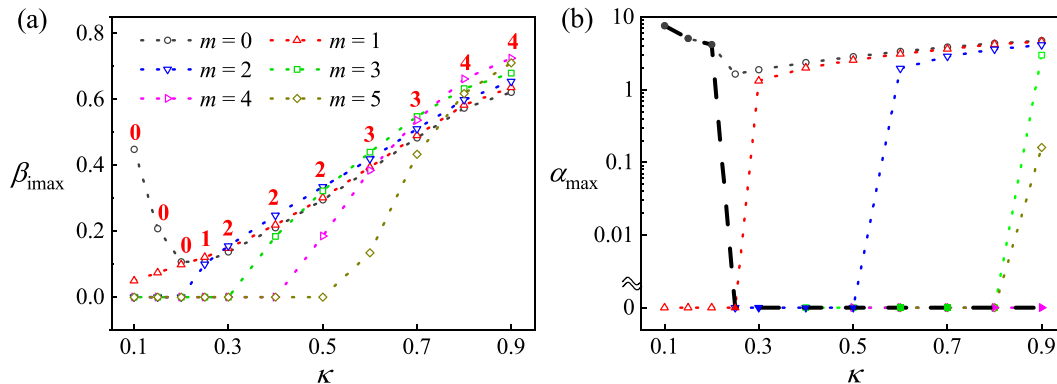


FIG. 7. (a) Maximum perturbation growth rate β_{\max} for different azimuthal modes as κ varies. The predominant mode is indicated by the red numbers. (b) Most unstable wavenumber α_{\max} for different azimuthal modes as κ varies. The most unstable wavenumbers corresponding to the predominant mode at different κ are denoted by the solid symbols and connected by the black thick dashed line.

However, β_{\max} keeps increasing as κ exceeds the critical values for modes $m = 1$ to 5 . Comparing the values of β_{\max} between different azimuthal modes, we can obtain the predominant mode under different κ , as shown by the red numbers in Fig. 7(a). Overall, the increase in κ can lead to the predominant mode transition from the axisymmetric mode to the helical modes with larger azimuthal wavenumbers. The variation of the most unstable wavenumber is shown in Fig. 7(b).

With the increase in κ , the value of α_{\max} for the axisymmetric mode decreases first and then increases, whereas those of helical modes keep constant first and then increase suddenly. The most unstable wavenumbers α_{\max} corresponding to the predominant mode are highlighted with solid symbols and connected with the black thick dashed line. For the predominant mode, the values of α_{\max} decrease significantly and finally maintain at zero with the increase in κ .

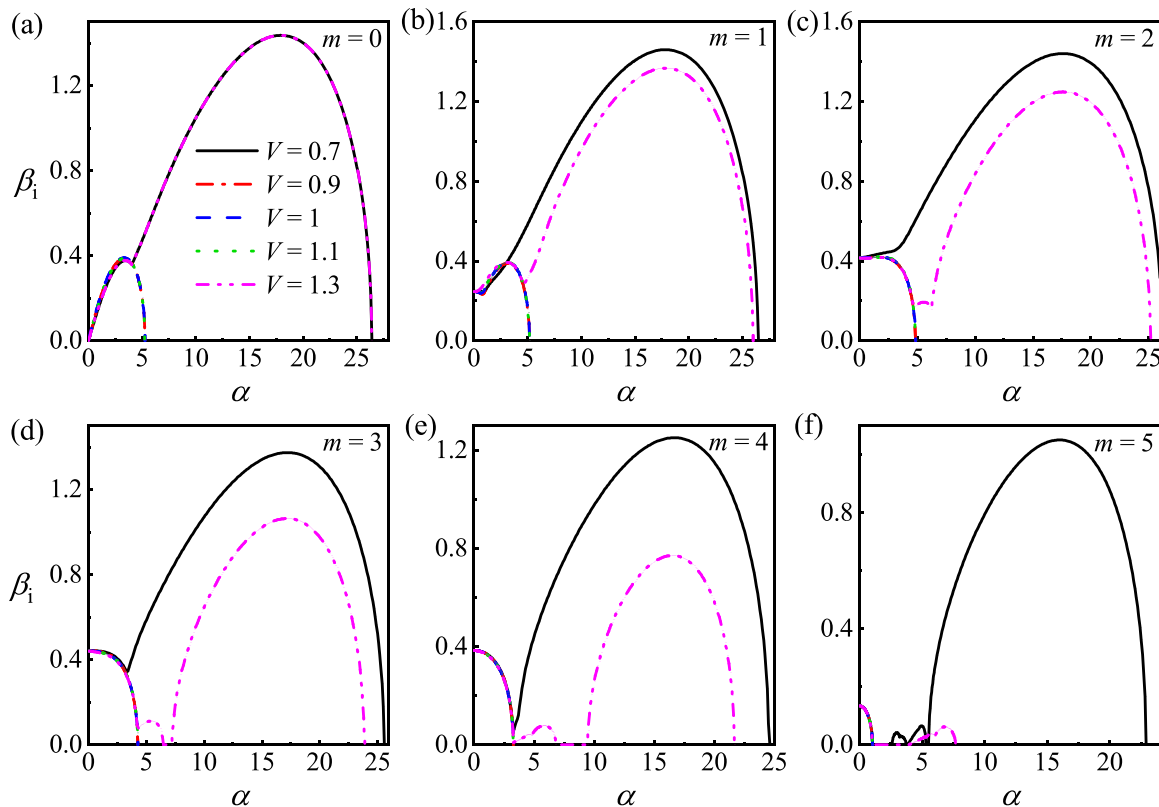


FIG. 8. Perturbation growth rate β_i vs wavenumber α for different azimuthal modes as V gradually changes ($V = 0.7, 0.9, 1, 1.1$, and 1.3 , respectively): (a) $m = 0$, (b) $m = 1$, (c) $m = 2$, (d) $m = 3$, (e) $m = 4$, and (f) $m = 5$.

D. Effect of the velocity ratio V

The velocity ratio V represents the axial velocity difference between the inner jet and the annular jet. Figures 8(a)–8(f) show the perturbation growth rates β_i for azimuthal modes $m = 0$ –5 as V changes. For the axisymmetric mode shown in Fig. 8(a), the growth rate curves under $V = 0.9, 1$, and 1.1 almost coincide with each other, indicating that the relatively weak axial KH instability of the inner interface has little effect on the jet breakup as V is rather close to 1. The growth rate curve of $V = 0.7$ almost coincides with that of $V = 1.3$. However, the cutoff wavenumbers, the maximum growth rates, and the most unstable wavenumbers of $V = 0.7$ and 1.3 are much larger than those of $V = 0.9, 1$, and 1.1 . Since the axial KH instability is more crucial as V diverges from 1, these results suggest that the enhancement of the axial KH instability brings in more perturbation with smaller wavelength into instability, promotes the jet breakup, and leads to the formation of smaller droplets. For helical modes $m = 1$ –5 shown in Figs. 8(b)–8(f), the growth rate curves of $V = 0.9, 1$, and 1.1 almost coincide with each other, whereas the cutoff wavenumbers, the maximum growth rates, and the most unstable wavenumbers of $V = 0.7$ and 1.3 are much larger than those of $V = 0.9, 1$, and 1.1 , respectively, which is similar to the situation of $m = 0$. However, there is an obvious difference between the growth rate curves of $V = 0.7$ and 1.3 . The cutoff wavenumbers and the maximum growth rates of $V = 0.7$ are larger than those of $V = 1.3$. As m increases, more

deviations of $\alpha_{\text{cut-off}}$ and β_{imax} between $V = 0.7$ and $V = 1.3$ can be observed. The tendencies of the most unstable wavenumbers α_{max} of modes $m = 1$ –5 between $V = 0.7$ and 1.3 are different. For $m = 1$ –4, the values of α_{max} almost equal each other between $V = 0.7$ and 1.3 . However, at $m = 5$, the most unstable wavenumber of $V = 1.3$ is much smaller than that of $V = 0.7$.

The maximum growth rates β_{imax} and the most unstable wavenumbers α_{max} for different azimuthal modes as V gradually changes from 0.5 to 1.5 are given in Figs. 9(a) and 9(b), respectively. It can be seen from Fig. 9(a) that the change of V has little effect on jet instability as V approaches 1. Specifically, the values of β_{imax} change slightly for modes $m = 0$ –3 as $0.8 \leq V \leq 1.1$ and for modes $m = 4$ and 5 as $0.8 \leq V \leq 1.3$. As V keeps decreasing from 0.7 or increasing from 1.3, the values of β_{imax} for each mode increase rapidly. The red numbers in Fig. 9(a) demonstrate the predominant modes. When V diverges from 1, the mode with smaller m tends to become the predominant mode, indicating that the enhancement of the axial KH instability of the inner interface can promote the instability mode with a lower azimuthal wavenumber. In Fig. 9(b), it is clear that V plays a dual effect on the variation of α_{max} . For each mode, the minimum value of α_{max} occurs as V approaches 1. The most unstable wavenumbers of the predominant modes at different V are highlighted by the solid symbols and also connected with the black thick dashed line. Overall, the coaxial jet presents an infinite wavelength as $\alpha_{\text{max}} = 0$ at $V = 1$ and 1.1 , whereas it presents

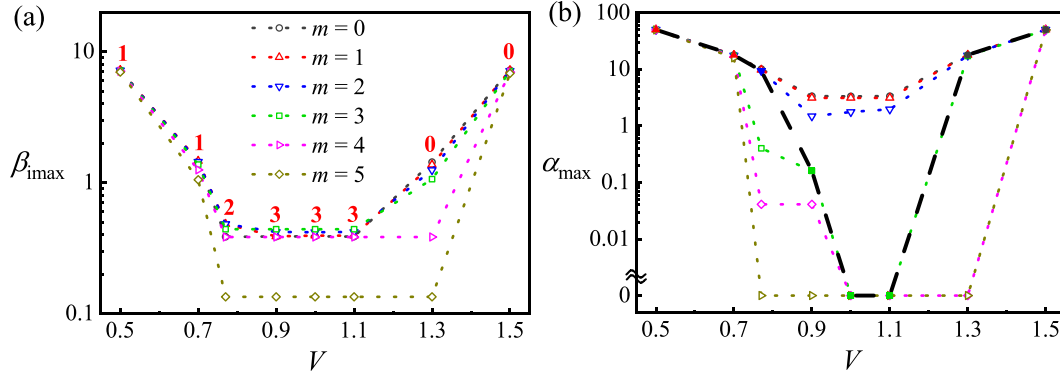


FIG. 9. Maximum perturbation growth rate β_{\max} for different azimuthal modes as V varies. The predominant mode is indicated by the red numbers. (b) Most unstable wavenumber α_{\max} for different azimuthal modes as V changes. The most unstable wavenumbers corresponding to the predominant mode at different V are denoted by the solid symbols and connected by the black thick dashed line.

much shorter wavelength as $\alpha_{\max} \sim O(10^1)$ when V diverges from 1, showing the typical characteristic of the Taylor breakup.

E. Effect of the velocity ratio W

The velocity ratio W represents the axial velocity difference between the outermost surrounding fluid and the annular liquid jet.

Figures 10(a)–10(f) show the perturbation growth rates β_i for modes $m = 0$ –5 at various W . For each mode, it is clear that the perturbation curves almost coincide together at relatively low W (e.g., $W \leq 2$), indicating that the relatively weak axial KH instability of the outer interface only has little effect on the growth of perturbation. However, as W keeps increasing, the cutoff wavenumber, the maximum growth rate, and the most unstable wavenumber of each mode increase

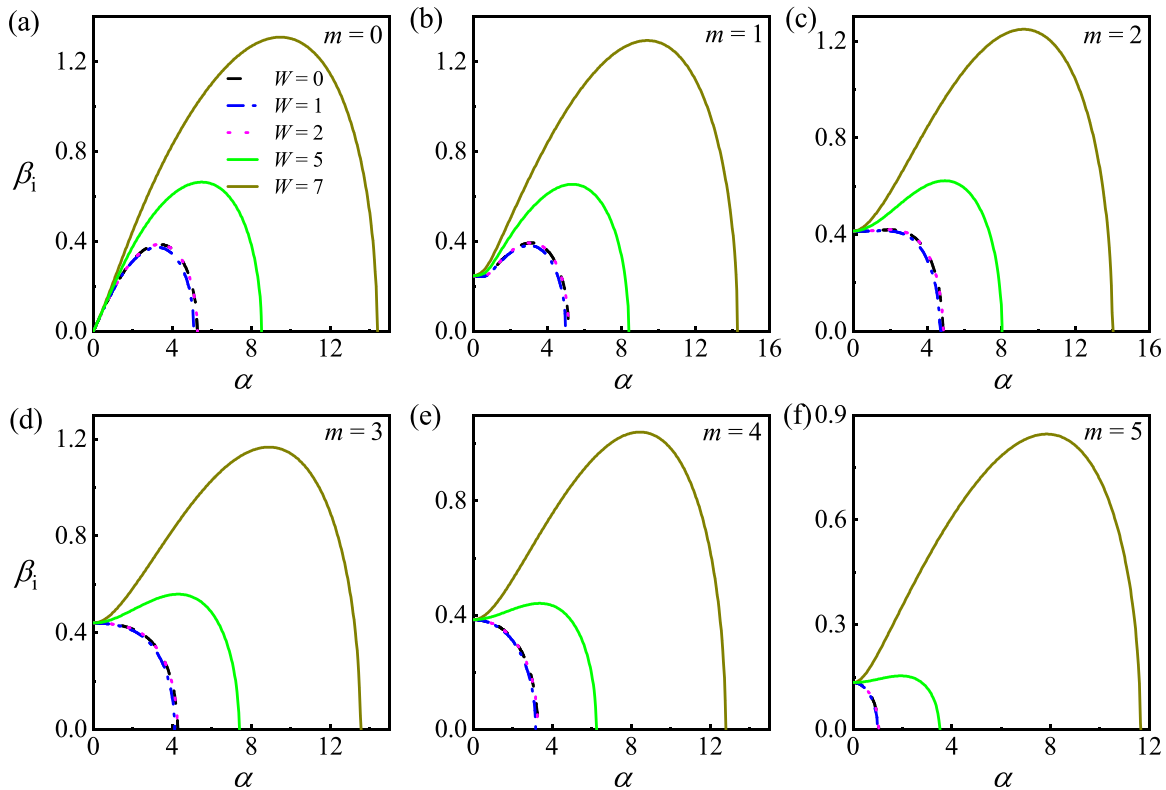


FIG. 10. Perturbation growth rate β_i vs wavenumber α for different azimuthal modes as W changes ($W = 0, 0.5, 1, 1.5, 2$, and 7 , respectively): (a) $m = 0$, (b) $m = 1$, (c) $m = 2$, (d) $m = 3$, (e) $m = 4$, and (f) $m = 5$.

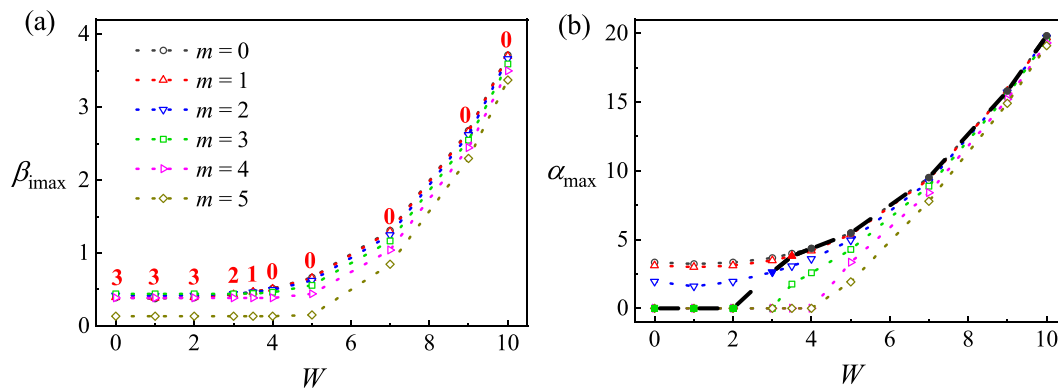


FIG. 11. Maximum perturbation growth rate β_{\max} for different azimuthal modes as W varies. The predominant mode is indicated by the red numbers. (b) Most unstable wavenumber α_{\max} for different azimuthal modes as W changes. The most unstable wavenumbers corresponding to the predominant mode at different W are denoted by the solid symbols and connected by the black thick dashed line.

dramatically, showing that the enhancement of the axial KH instability brings in more perturbation with smaller wavelength into instability, promotes the jet breakup, and leads to the formation of much smaller droplets.

The maximum perturbation growth rates β_{\max} and the most unstable wavenumbers α_{\max} for modes $m = 0-5$ as W gradually changes from 0 to 10 are depicted in Fig. 11. It can be observed in Fig. 11(a) that the increase in W has little effect on the values of β_{\max} as $W \leq 4$. Once W gets further larger, an increase in W leads to an obvious increase in β_{\max} for each mode, suggesting that the enhancement of the axial KH instability on the outer interface has a remarkable destabilizing effect on the coaxial swirling jet. The predominant modes at different W are denoted by the red numbers, as shown in Fig. 11(a). It is found that a larger value of W leads to the predominant mode with a smaller azimuthal wavenumber m . The corresponding most unstable wavenumbers of each mode are plotted in Fig. 11(b). It is found that the variation tendency of α_{\max} at different W is similar to that of the maximum growth rates. The values of α_{\max} for each mode keep almost unchanged at first as W increases from 0 to 4. Once $W > 4$, α_{\max} increases quickly with the increase in W . The most unstable wavenumbers of the predominant modes at different W are identified with solid symbols and connected with the black thick dashed line. It is obvious that the most unstable wavenumber of the predominant mode keeps certain at zero first (i.e., $0 \leq W \leq 2$) and then increases significantly with the increase in W .

F. Effect of azimuthal velocity jump

The parameter Δ reflects the degree of azimuthal velocity jump at the inner interface. As the variation of Δ affects the centrifugal instability, the azimuthal KH instability, and the instability caused by the Coriolis force simultaneously, the effect of Δ on the jet instability characteristics can be very complex. Figures 12(a)–12(f) show the perturbation growth rates β_i for azimuthal modes $m = 0-5$ as Δ changes. For each mode, the maximum growth rates first decrease and then increase as Δ increases from 0 to 1.4, indicating that Δ has a dual effect on the jet instability. The effects of Δ on the variations of the cutoff wavenumbers and the most unstable wavenumbers are very complex. Specifically, the cutoff wavenumbers and the most unstable

wavenumbers first decrease and then increase for modes $m = 0-3$, as shown in Figs. 12(a)–12(d). However, multiple variation tendencies of the cutoff wavenumbers and the most unstable wavenumbers with Δ changing can be observed for modes $m = 4$ and 5, as shown in Figs. 12(e)–12(f), respectively.

The maximum growth rates β_{\max} and the most unstable wavenumbers α_{\max} for modes $m = 0-5$ as Δ changes are displayed in Figs. 13(a) and 13(b), respectively. The variation of Δ has a dual effect on β_{\max} , and the minimum values of β_{\max} for each mode occur at the range of $0.6 \leq \Delta \leq 0.8$, as shown in Fig. 13(a). The red numbers indicate the predominant modes at different values of Δ . Different from the effects of other parameters, it is found that the transitions of azimuthal modes are not consecutive as Δ gradually increases from 0 to 1.6. Specifically, the predominant mode maintains $m = 5$ as $\Delta \leq 0.4$ and changes to $m = 1$ and 0 at $\Delta = 0.5$ and 0.6, respectively. As Δ increases from 0.7 to 1.6, the predominant mode shifts continuously from $m = 2$ to 5. The mechanism of mode transition can be explained through the competition of different instability mechanisms. As mentioned before, the azimuthal KH instability, the centrifugal instability, and the instability caused by the Coriolis force are all active if $\Delta < 1$. When $\Delta = 0$, the effects of centrifugal instability and the azimuthal KH instability are the strongest due to the sharpest decrease in the azimuthal velocity at the inner interface. Therefore, the values of β_{\max} are relatively large for each mode and the azimuthal mode with larger wavenumber (i.e., $m = 5$) can dominate the jet instability. The centrifugal instability and the azimuthal KH instability get weakened as Δ increases from 0 to 1. However, the increase in Δ also leads to an enhanced swirling of the annular jet, leading to the strengthened Coriolis force of the coaxial jet. The competition of these mechanisms is the main cause of the non-monotonic and discontinuous variation of β_{\max} . The azimuthal KH instability and the centrifugal instability disappear as $\Delta = 1$. As Δ gets larger than 1, the azimuthal KH instability and the Coriolis instability increase with the increase in Δ , thus leading to the continuous increase in β_{\max} for each mode and the transition of predominant modes with larger m . The evolutions of α_{\max} for each azimuthal mode are very complex, as shown in Fig. 13(b). The most unstable wavenumbers of the predominant modes as Δ changes are highlighted with solid symbols and connected with the black bold dashed line. Generally, the values of α_{\max} of the predominant mode

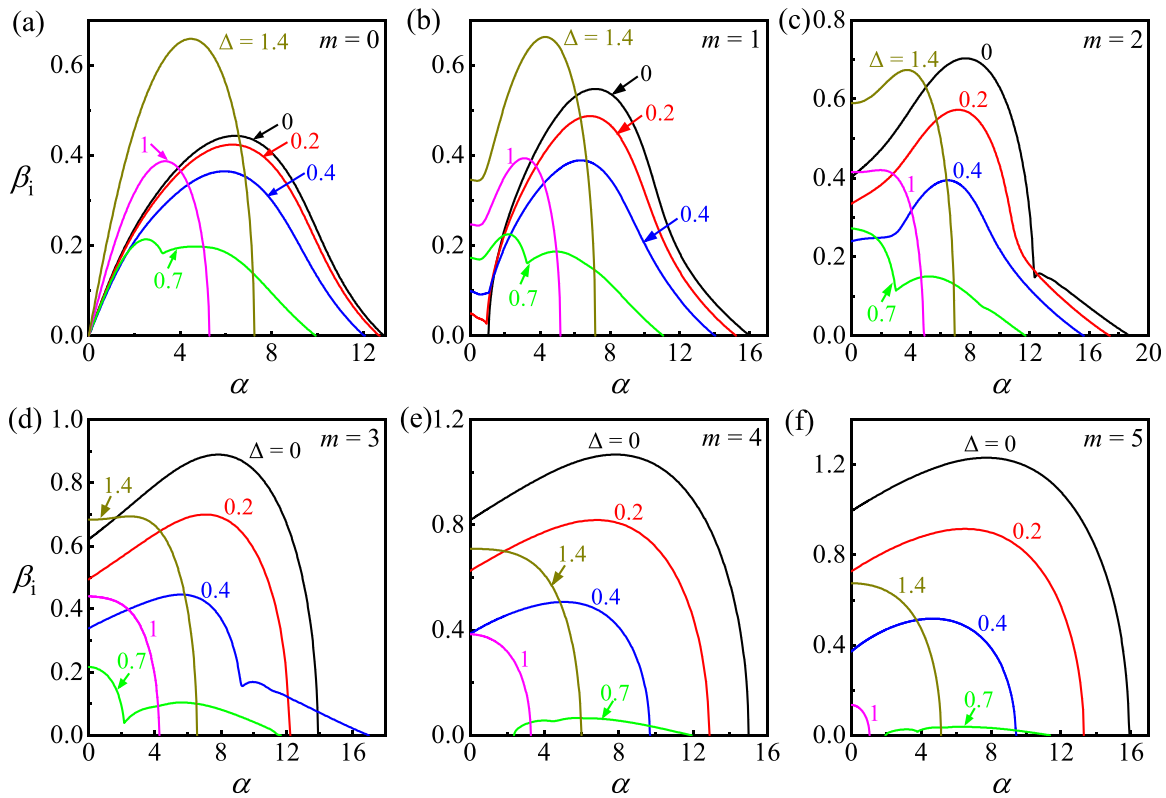


FIG. 12. Perturbation growth rate β_i vs wavenumber α for different azimuthal modes as Δ changes ($\Delta = 0, 0.2, 0.4, 0.6, 0.8, 1$, and 1.4): (a) $m = 0$, (b) $m = 1$, (c) $m = 2$, (d) $m = 3$, (e) $m = 4$, and (f) $m = 5$.

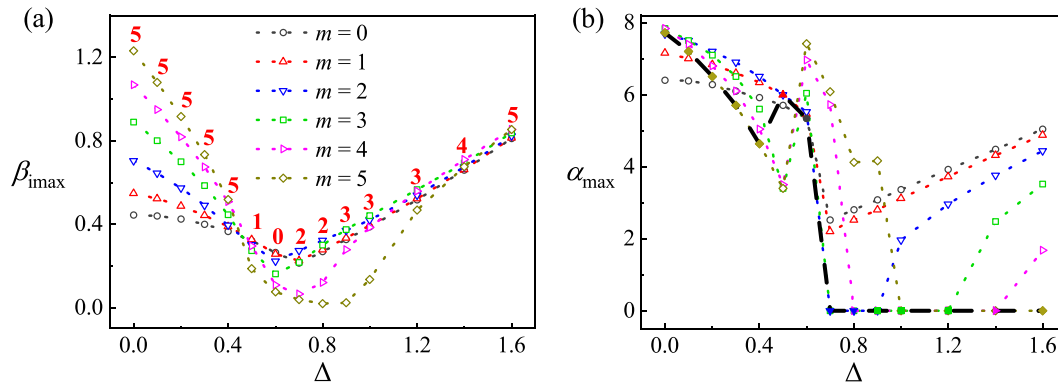


FIG. 13. (a) Maximum perturbation growth rate β_{\max} for different azimuthal modes as Δ varies, where the predominant mode is indicated by the red numbers. (b) Most unstable wavenumber α_{\max} for different azimuthal modes as Δ changes. The most unstable wavenumbers corresponding to the predominant mode at different Δ are denoted by the solid symbols and connected by the black thick dashed line.

present an overall decreasing tendency with the increase in Δ as $0 \leq \Delta \leq 0.7$ and keep constant at zero as $\Delta > 0.7$.

G. Phase diagram of mode transition

In order to gain more details on the mechanism of mode transition, the phase diagrams of azimuthal modes with different m are given in Fig. 14, where the swirling ratio S and the Weber number We

are chosen as the characteristic parameters. Without the loss of generality, S varies within the range of $O(1)$ and We changes within the ranges of $O(1-10^2)$. The variation of the jet radius ratio κ ($=0.4, 0.6$, and 0.8) is also considered, as shown by the comparison of results between Figs. 14(a), 14(b), and 14(c), respectively. Other parameters are kept at the reference state. For a certain value of κ , it is found that an increase in either S or We can promote the continuous transition of

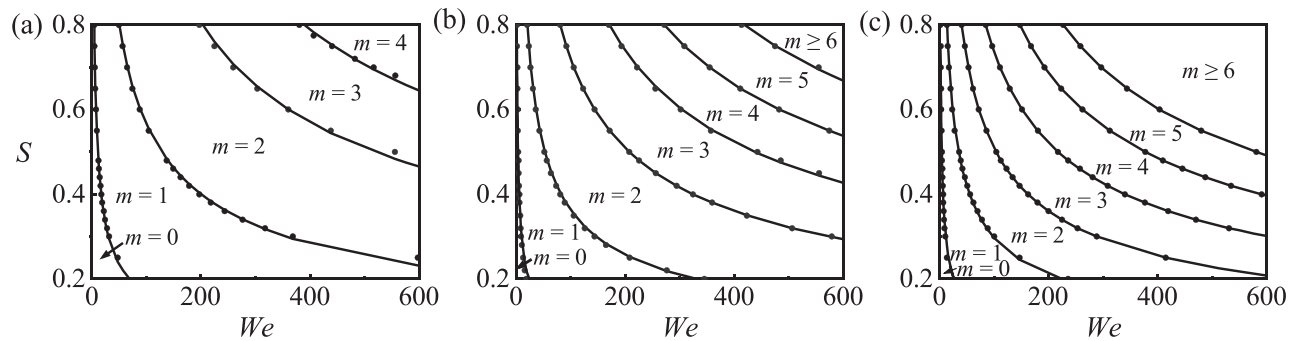


FIG. 14. Phase diagrams of the azimuthal instability modes on the We - S space under different values of κ , where (a) $\kappa = 0.4$, (b) $\kappa = 0.6$, and (c) $\kappa = 0.8$. The solid symbols denote the theoretical boundaries, and the lines denote the fitting curves with the form $We \cdot S^2 = C$, where C is a constant with its value depending on κ and m .

TABLE I. Specific values of C under different values of κ and m .

κ	$m = 0/1$	$m = 1/2$	$m = 2/3$	$m = 3/4$	$m = 4/5$	$m = 5/6$
0.4	2.74	31.99	129.66	249.11
0.6	0.91	13.20	51.84	109.36	173.60	267.47
0.8	1.04	8.85	25.94	54.34	94.30	145.06

predominate mode to larger azimuthal wavenumber m . Comparing the transition boundaries under different κ , it is observed that an increase in κ leads to an earlier mode transition. These tendencies are similar to those observed from Figs. 3, 5, and 7, respectively. Figure 14 also indicates that the transition boundaries between different modes satisfy the fitting curves of $We \cdot S^2 = C$ approximately, where C is a constant. The fitting curves are shown by the solid lines, and the specific values of C are decided by the values of κ and azimuthal wavenumber m , as shown in Table I. It is found that the values of C increase significantly as the jet instability gradually trans to helical modes larger m . However, the values of C decrease with the increase in κ . It is worth noting that C can be expressed as the form $C = \rho_2 \Omega^2 R_2^3 / \gamma_2$, which is the reciprocal of the Hocking number defined in the previous study.²⁶ As C represents the ratio of the centrifugal force to the surface tension force, it can be inferred that the mode transition is triggered by the centrifugal force. Overall, the transition from mode $m=0$ to 1 occurs as $C \sim O(1)$, which indicates that the coaxial jet loses its axisymmetry as the centrifugal force overcomes the surface tension force. The continuous transitions of helical modes with different m (from 1–5) occur as $C \sim O(10^1-10^2)$, showing a secondary effect of surface tension on the helical modes.

IV. CONCLUSION

An analytical model for the linear temporal instability of an inviscid coaxial swirling liquid jet in outermost gas surroundings is established in this work, where the circumferential Rankine vortex and the axial discontinuous velocities are assumed as the basic flow. The normal mode method is utilized to inspect the perturbation growth of the jet, and the dispersion relation of perturbation is verified by simplifying the coaxial swirling jet model and comparing it with the previous results. A parametric study is performed to investigate the effect of the controlling parameters on the jet instabilities of the axisymmetric mode with $m=0$ and helical modes with $m=1-5$. The main

parameters include the swirling ratio S , the Weber number We , the radius ratio κ , the velocity ratio V between the inner jet and the annular jet, the velocity ratio W between the surrounding fluid and the annular jet, and the azimuthal velocity jump Δ . Predominant modes, which decide the jet instability, are identified to show the transition between different azimuthal modes. It is found that the increase in the swirling ratio S can enhance the Coriolis instability caused by the rotation of the vortex core, thus causing an increase in the maximum perturbation growth rates of each mode and continuous transition of predominate mode from $m=0$ to 5. The Weber number We reflects the relative importance between the axial inertia force and the interfacial tension. The increase in We is found to have a dual effect on the instability of the axisymmetric mode but enhance the instability of helical modes. It is also found that the predominate mode gradually trans to larger m with We increasing. The effect of κ on the jet instability is similar to that of S as κ represents the size of the swirling vortex core. An increase in κ can promote the occurrence of azimuthal mode with larger m . The velocity ratios V and W mainly affect the axial KH instability of the inner and outer jet interfaces, respectively. When V and W gradually diverge from 1, the instability of the jet will be enhanced and droplets with much smaller size can be formed. An increase in the axial KH instability also leads to the predominate mode with smaller m . The parameter Δ , which reflects the azimuthal velocity jump, can affect the azimuthal KH instability, the centrifugal instability, and the instability caused by the Coriolis force simultaneously. The competition between different instability mechanisms leads to a non-monotonic and discontinuous transition of predominate modes as Δ varies. Finally, phase diagrams of mode transition on the We - S plane under different values of κ are displayed, showing that the transition between different azimuthal modes is mainly affected by the relative importance between the centrifugal force and the interfacial tension. This study is expected to provide guidance for the physical mechanisms on the instability of the coaxial swirling jet in various applications.

ACKNOWLEDGMENTS

This work was supported by the National Natural Science Foundation of China (Nos. 12272372, 11902318, and 12027801), the Youth Innovation Promotion Association CAS (Nos. 2018491 and 2023477), and the Fundamental Research Funds for the Central Universities.

AUTHOR DECLARATIONS

Conflict of Interest

The authors have no conflicts to disclose.

Author Contributions

Yiqian Xu: data curation (equal); formal analysis (equal); investigation (equal); methodology (equal); visualization (equal); and writing – original draft (equal). **Kai Mu:** conceptualization (equal); formal analysis (equal); funding acquisition (equal); supervision (equal); and writing – review and editing (equal). **Ran Qiao:** data curation (equal); formal analysis (equal); and methodology (equal). **Yanfeng Wu:** investigation (equal); software (equal); and supervision (equal). **Ting Si:** conceptualization (equal); funding acquisition (equal); investigation (equal); project administration (equal); supervision (equal); and writing – review and editing (equal).

DATA AVAILABILITY

The data that support the findings of this study are available from the corresponding author upon reasonable request.

APPENDIX: DERIVATION OF THE DISPERSION RELATION

For the inner jet region of $0 < r \leq R_1$, taking Eq. (23) into Eqs. (15) and (16), the governing equations are given by

$$\hat{v}_1'(r) + r^{-1}\hat{v}_1(r) + imr^{-1}\hat{w}_1(r) + ik\hat{u}_1(r) = 0, \quad (\text{A1})$$

$$f_1\hat{u}_1(r) = \rho_1^{-1}k\hat{p}_1(r), \quad (\text{A2})$$

$$if_1\hat{v}_1(r) + 2\Omega\hat{w}_1(r) = \rho_1^{-1}\hat{p}_1'(r), \quad (\text{A3})$$

$$if_1\hat{w}_1(r) - 2\Omega\hat{v}_1(r) = (\rho_1 r)^{-1}im\hat{p}_1(r), \quad (\text{A4})$$

where $f_1 = \omega - kU_1 - m\Omega$.

Combining Eqs. (A1)–(A4), the disturbance of pressure can be derived as

$$r^2\hat{p}_1''(r) + r\hat{p}_1'(r) + [k^2r^2(4\Omega^2f_1^{-2} - 1) - m^2]\hat{p}_1(r) = 0, \quad (\text{A5})$$

where $\hat{p}_1''(r) = \frac{d^2\hat{p}_1(r)}{dr^2}$ and $\hat{p}_1'(r) = \frac{d\hat{p}_1(r)}{dr}$. The general solution of Eq. (A5) is

$$\hat{p}_1(r) = A_1J_m(\beta_1r) + B_1Y_m(\beta_1r), \quad (\text{A6})$$

where J_m , Y_m are the first and the second kinds of Bessel functions with order m , and $\beta_1^2 = k^2(4\Omega^2f_1^{-2} - 1)$, respectively. Since Y_m grows exponentially as $r \rightarrow 0$, one must have $B_1 = 0$ according to the boundary condition Eq. (17). Combining Eq. (A6) with Eqs. (A1)–(A4), the expressions of $\hat{v}_1(r)$ can be derived as

$$\hat{v}_1(r) = i(\rho_1 f_1)^{-1}k^2\beta_1^{-2}A_1(-2m\Omega r^{-1}f_1^{-1}J_m(\beta_1r) + \beta_1J_m'(\beta_1r)). \quad (\text{A7})$$

For the region of annular jet and surrounding fluid where $r > R_1$, as the flow is irrotational, the velocity potential function ϕ is introduced with $\hat{\mathbf{u}}_i = \nabla\phi_i$ ($i = 2, 3$), where ϕ_i is also expressed with the form

$$\phi_i = \varphi_i(r)e^{i(kz+m\theta-\omega t)}. \quad (\text{A8})$$

Subscribing Eq. (A8) into the mass-conservation equation of Eq. (15), $\Delta\phi_i = 0$ can be obtained consequently, which can be further written as

$$r^2\varphi_i''(r) + r\varphi_i'(r) - (m^2 + k^2r^2)\varphi_i(r) = 0, \quad (\text{A9})$$

where $\varphi_i''(r) = \frac{d^2\varphi_i(r)}{dr^2}$ and $\varphi_i'(r) = \frac{d\varphi_i(r)}{dr}$. The general solution of Eq. (A9) is $\varphi_i(r) = A_iI_m(kr) + B_iK_m(kr)$, where I_m , K_m are the first and the second kinds of modified Bessel functions with order m , respectively. Since Y_m grows exponentially as $r \rightarrow \infty$, one must have $A_3 = 0$. Substituting the velocity potential function into $\mathbf{u}_i = \Delta\phi_i$, the disturbed velocities can be written as

$$\hat{u}_2(r) = ik(A_2I_m(kr) + B_2K_m(kr)), \quad (\text{A10})$$

$$\hat{v}_2(r) = k(A_2I_m'(kr) + B_2K_m'(kr)), \quad (\text{A11})$$

$$\hat{u}_3(r) = ikB_3K_m(kr), \quad (\text{A12})$$

$$\hat{v}_3(r) = kB_3K_m'(kr). \quad (\text{A13})$$

The momentum equation in the axial direction is given by

$$\left(\omega - kU_i - \frac{m\Omega R_i^2\Delta}{r^2}\right)\hat{u}_i(r) = \rho_i^{-1}k\hat{p}_i(r), \quad i = 2, 3. \quad (\text{A14})$$

By substituting Eqs. (A10) and (A12) into Eq. (A14), the expressions of $\hat{p}_2(r)$ and $\hat{p}_3(r)$ can be obtained as

$$\hat{p}_2(r) = -i\rho_2\left(-\omega + kU_2 + \frac{m\Omega R_1^2\Delta}{r^2}\right)(A_2I_m(kr) + B_2K_m(kr)), \quad (\text{A15})$$

$$\hat{p}_3(r) = -i\rho_3\left(-\omega + kU_3 + \frac{m\Omega R_1^2\Delta}{r^2}\right)B_3K_m(kr). \quad (\text{A16})$$

The coefficients A_1 , A_2 , B_2 , B_3 can be determined by the boundary conditions. Through the displacement continuity condition at the inner interface, we can get

$$\hat{v}_1(R_1^-) = -if_1\hat{\eta}_1. \quad (\text{A17})$$

Substituting Eq. (A7) into Eq. (A17), A_1 can be decided as

$$A_1 = -\frac{f_1^3\beta_1^2\rho_1R_1\hat{\eta}_1}{k^2G}, \quad (\text{A18})$$

where $G = f_1\beta_1R_1J_m'(\beta_1R_1) - 2m\Omega J_m(\beta_1R_1)$.

Similarly, for the annular jet, we can obtain the disturbed velocity as

$$\hat{v}_2(R_1^+) = -if_{21}\hat{\eta}_1, \quad (\text{A19})$$

where $f_{21} = \omega - kU_2 - m\Delta\Omega$. Considering the boundary conditions for the outer interface, we can get

$$\hat{v}_2(R_2^-) = -if_{22}\hat{\eta}_2, \quad (\text{A20})$$

where $f_{22} = \omega - kU_2 - m\Delta\Omega\frac{R_1^2}{R_2^2}$. Combining Eqs. (A11), (A19), and (A20), A_2 and B_2 can be decided as

$$A_2 = \frac{i}{kH_1}(f_{21}K_m'(kR_2)\hat{\eta}_1 - f_{22}K_m'(kR_1)\hat{\eta}_2), \quad (\text{A21})$$

$$B_2 = \frac{i}{kH_1} (-f_{21}I'_m(kR_2)\hat{\eta}_1 + f_{22}I'_m(kR_1)\hat{\eta}_2), \quad (\text{A22})$$

where $H_1 = I'_m(kR_2)K'_m(kR_1) - I'_m(kR_1)K'_m(kR_2)$.

For the driving fluid, we have

$$\hat{\nu}_3(R_2^+) = -if_3\hat{\eta}_2, \quad (\text{A23})$$

where $f_3 = \omega - kU_3 - m\Omega\Delta\frac{R_1^2}{R_2^2}$. Substituting Eq. (A13) into Eq. (A23), B_3 is decided by

$$B_3 = -\frac{if_3\hat{\eta}_2}{kK'_m(kR_2)}. \quad (\text{A24})$$

Combining the expression of the pressure and the coefficients (A_1, A_2, B_2, B_3) with the dynamic boundary condition, the following relationship can be derived:

$$\frac{\hat{\eta}_2}{\hat{\eta}_1} = [K_m(kR_1)I'_m(kR_1) - K'_m(kR_1)I_m(kR_1)]^{-1} \{H_1T_1 + f_{21}(f_{22})^{-1}[I'_m(kR_2)K_m(kR_1) - K'_m(kR_2)I_m(kR_1)]\}, \quad (\text{A25})$$

$$\frac{\hat{\eta}_1}{\hat{\eta}_2} = [K_m(kR_2)I'_m(kR_2) - K'_m(kR_2)I_m(kR_2)]^{-1} \{H_1T_2 + f_{22}(f_{21})^{-1}[I'_m(kR_1)K_m(kR_2) - K'_m(kR_1)I_m(kR_2)]\}, \quad (\text{A26})$$

where

$$T_1 = \frac{k}{\rho_2 f_{21} f_{22}} \left[\gamma_1 \left(\frac{m^2 - 1}{R_1^2} + k^2 \right) + \frac{f_1^3 \beta_1^2 \rho_1 R_1}{k^2 G} J_m(\beta_1 R_1) - \Omega^2 R_1 (-\rho_2 \Delta^2 + \rho_1) \right],$$

$$T_2 = \frac{k}{\rho_2 f_{21} f_{22}} \left[\gamma_2 \left(\frac{m^2 - 1}{R_2^2} + k^2 \right) + \frac{\rho_3 f_3^2 K_m(kR_2)}{k K'_m(kR_2)} - \frac{\Omega^2 R_1^4 \Delta^2}{R_2^3} (-\rho_3 + \rho_2) \right].$$

Simplifying Eqs. (A25) and (A26) into the dimensionless form, the dimensionless dispersion relation of Eq. (24) can be obtained.

REFERENCES

- P. Billant, J. M. Chomaz, and P. Huerre, "Experimental study of vortex breakdown in swirling jets," *J. Fluid Mech.* **376**, 183–219 (1998).
- K. Oberleithner, M. Sieber, C. N. Nayeri, C. O. Paschereit, C. Petz, H. C. Hege, B. R. Noack, and I. Wygnanski, "Three-dimensional coherent structures in a swirling jet undergoing vortex breakdown: Stability analysis and empirical mode construction," *J. Fluid Mech.* **679**, 383–414 (2011).
- Y. Ye, H. F. Liu, J. R. Li, T. Liu, J. J. Dong, B. Liu, C. H. Wu, Z. Y. Yue, and M. F. Yao, "A numerical investigation on the effects of intake swirl and mixture stratification on combustion characteristics in a natural-gas/diesel dual-fuel marine engine," *J. Therm. Sci.* **32**, 414–426 (2023).
- M. Sjerić, J. Krajnović, A. Vucetić, and D. Kozarac, "Influence of swirl flow on combustion and emissions in spark-ignition experimental engine," *J. Energy Eng.* **147**, 04021014 (2021).
- P. Balakrishnan and K. Srinivasan, "Reduction of jet impingement noise by addition of swirl," *ASME J. Vib. Acoust.* **138**, 061013 (2016).
- P. Balakrishnan and K. Srinivasan, "Influence of swirl number on jet noise reduction using flat vane swirlers," *Aerosp. Sci. Technol.* **73**, 256–268 (2018).
- L. Rayleigh, "On the instability of jets," *Proc. London Math. Soc.* **s1-10**, 4–13 (1878).
- L. Rayleigh, "On the instability of a cylinder of viscous liquid under capillary force," *Philos. Mag.* **34**, 145–154 (1892).
- C. Weber, "Zum zerfall eines flüssigkeitsstrahles," *Z. Angew. Math. Mech.* **11**, 136–154 (1931).
- G. I. Taylor, "Generation of ripples by wind blowing over a viscous fluid," in *The Scientific Papers of G. I. Taylor* (Cambridge University Press, Cambridge, 1962), Vol. 3, pp. 244–254.
- R. D. Reitz and F. V. Bracco, "Mechanism of breakup of round liquid jets," in *Encyclopedia of Fluid Mechanics* (Gulf Publishing Company, 1986), pp. 233–249.
- J. B. Keller, S. I. Rubinow, and Y. O. Tu, "Spatial instability of a jet," *Phys. Fluids* **16**, 2052–2055 (1973).
- S. J. Leib and M. E. Goldstein, "Convective and absolute instability of a viscous liquid jet," *Phys. Fluids* **29**, 952–954 (1986).
- S. J. Leib and M. E. Goldstein, "The generation of capillary instabilities on a liquid jet," *J. Fluid Mech.* **168**, 479–500 (1986).
- S. P. Lin, *Breakup of Liquid Sheets and Jets* (Cambridge University Press, 2003).
- J. Eggers and E. Villermaux, "Physics of liquid jets," *Rep. Prog. Phys.* **71**, 036601 (2008).
- J. C. Lasheras and E. J. Hopfinger, "Liquid jet instability and atomization in a coaxial gas stream," *Annu. Rev. Fluid Mech.* **32**, 275–308 (2000).
- P. Huerre and P. A. Monkewitz, "Local and global instabilities in spatially developing flows," *Annu. Rev. Fluid Mech.* **22**, 473–537 (1990).
- M. R. Khorrami, "On the viscous modes of instability of a trailing line vortex," *J. Fluid Mech.* **225**, 197–212 (1991).
- C. Olendrar, A. Sellier, M. Rossi, and P. Huerre, "Inviscid instability of the batchelor vortex: Absolute-convective transition and spatial branches," *Phys. Fluids* **11**, 1805–1820 (1999).
- I. Delbende, J. M. Chomaz, and P. Huerre, "Absolute/convective instabilities in the batchelor vortex: A numerical study of the linear impulse response," *J. Fluid Mech.* **355**, 229–254 (1998).
- T. Loiseleux, J. M. Chomaz, and P. Huerre, "The effect of swirl on jets and wakes: Linear instability of the rankine vortex with axial flow," *Phys. Fluids* **10**, 1120–1134 (1998).
- F. Gallaire and J. M. Chomaz, "Instability mechanisms in swirling flows," *Phys. Fluids* **15**, 2622–2639 (2003).
- R. N. Parthasarathy and K. Subramaniam, "Temporal instability of swirling gas jets injected in liquids," *Phys. Fluids* **13**, 2845–2850 (2001).
- D. J. Sun, G. H. Hu, Z. Gao, and X. Y. Yin, "Stability and temporal evolution of a swirling jet with centrifugally unstable azimuthal velocity," *Phys. Fluids* **14**, 4081–4084 (2002).
- J. Kubitschek and P. D. Weidman, "The effect of viscosity on the stability of a uniformly rotating liquid column in zero gravity," *J. Fluid Mech.* **572**, 261–286 (2007).
- P. Billant and F. Gallaire, "A unified criterion for the centrifugal instabilities of vortices and swirling jets," *J. Fluid Mech.* **734**, 5–35 (2013).
- C. Jacques, B. Pierro, F. Alizard, M. Buffat, A. Cadiou, and L. L. Penven, "Stability of variable density rotating flows: Inviscid case and viscous effects in the limit of large reynolds numbers," *Phys. Rev. Fluids* **8**, 033901 (2023).
- J. Panda and D. K. McLaughlin, "Experiments on the instabilities of a swirling jet," *Phys. Fluids* **6**, 263–276 (1994).
- J. P. Kubitschek and P. D. Weidman, "Helical instability of a rotating viscous liquid jet," *Phys. Fluids* **19**, 114108 (2007).
- T. L. Sahu, U. Chetan, J. Mahato, P. K. Kar, P. K. Das, and R. Lakkaraju, "Formation and breakup of twisting ligaments in a viscous swirling liquid jet," *Phys. Fluids* **34**, 112118 (2022).
- S. Schmidt and K. Oberleithner, "Global modes of variable-viscosity two-phase swirling flows and their triadic resonance," *J. Fluid Mech.* **955**, A24 (2023).
- A. Kageyama and Y. Goto, "Formation of twisted liquid jets," *Phys. Rev. Fluids* **5**, 064002 (2020).
- D. T. A. Jordan, N. M. Ribe, A. Deblais, and D. Bonn, "Chain oscillations in liquid jets," *Phys. Rev. Fluids* **7**, 104001 (2022).
- H. Soni, "Taylor's chiral microswimmer," *Phys. Rev. Fluids* **8**, 044201 (2023).
- M. V. Panchagnula, P. E. Sojka, and P. J. Santangelo, "On the three-dimensional instability of a swirling, annular, inviscid liquid sheet subject to unequal gas velocities," *Phys. Fluids* **8**, 3300–3312 (1996).

- ³⁷Y. Liao, S. M. Jeng, M. A. Jog, and M. A. Benjamin, "Instability of an annular liquid sheet surrounded by swirling airstreams," *AIAA J.* **38**, 453–460 (2000).
- ³⁸K. Yan, M. Lü, Z. Ning, and Y. C. Song, "Linear instability analysis of an annular swirling viscous liquid jet," *Appl. Mech. Mater.* **66–68**, 1556–1561 (2011).
- ³⁹K. Yan, Z. Ning, M. Lü, C. H. Sun, J. Fu, and Y. X. Li, "Spatial instability in annular swirling viscous liquid sheet," *Phys. Fluids* **27**, 024101 (2015).
- ⁴⁰K. Liu, D. J. Sun, and X. Y. Yin, "Instability of gas/liquid coaxial jet," *J. Hydrodyn.* **19**, 542–550 (2007).
- ⁴¹S. B. Li, R. Yang, X. S. Luo, and T. Si, "Instability study of an electrified coaxial jet in a coflowing gas stream," *Chin. J. Theor. Appl. Mech.* **49**, 997–1007 (2017).
- ⁴²M. A. Herrada, A. M. Gañán-Calvo, and P. Guillot, "Spatiotemporal instability of a confined capillary jet," *Phys. Rev. E* **78**, 046312 (2008).
- ⁴³M. A. Herrada, J. M. Montanero, C. Ferrera, and A. M. Gañán-Calvo, "Analysis of the dripping-jetting transition in compound capillary jets," *J. Fluid Mech.* **649**, 523–536 (2010).
- ⁴⁴F. Li, X. Y. Yin, and X. Z. Yin, "Instability of a viscous coflowing jet in a radial electric field," *J. Fluid Mech.* **596**, 285–311 (2008).
- ⁴⁵D. Joseph, J. Wang, and T. Funada, *Potential Flows of Viscous and Viscoelastic Liquids* (Cambridge University Press, 2007).
- ⁴⁶T. Funada and D. D. Joseph, "Viscous potential flow analysis of capillary instability," *Int. J. Multiphase Flow* **28**, 1459–1478 (2002).
- ⁴⁷R. Qiao, K. Mu, and T. Si, "Analytical instability theory of a liquid jet under a thermal field," *Acta Mech. Sin.* **39**, 323086 (2023).